Journal of the Indian Chemical Society 102 (2025) 101702

Contents lists available at ScienceDirect

Journal of the Indian Chemical Society

journal homepage: www.journals.elsevier.com/journal-of-the-indian-chemical-society

A comprehensive investigation into the spectroscopic properties, solvent effects on electronic properties, structural characteristics, topological insights, reactive sites, and molecular docking of racecadotril: A potential antiviral and antiproliferative agent

R. Manjula [a,b], C. Pavithra [a,**], A. Ram Kumar [c], K. Durgadevi [d], Babu Balraj [e], S. Selvaraj [f,*]

[a] PG and Research Department of Physics, Marudhar Kesari Jain College for Women, Vaniyambadi, 635751, Tamil Nadu, India
[b] Department of Physics, Sri Aandal Arts and Science College for Women, Kilmurungai, Ambur, 635 812, Tamil Nadu, India
[c] Department of Biotechnology, Saveetha School of Engineering, Saveetha Institute of Medical and Technical Sciences (SIMATS), Chennai, 602105, Tamil Nadu, India
[d] PG and Research Department of Physics, Arignar Anna Government Arts College, Cheyyar, 604407, Tamil Nadu, India
[e] Department of Physics, Vel Tech Rangarajan Dr. Sagunthala R&D Institute of Science and Technology, Chennai, 600062, Tamil Nadu, India
[f] Department of Physics, Saveetha School of Engineering, Saveetha Institute of Medical and Technical Sciences (SIMATS), Chennai, 602105, Tamil Nadu, India

ARTICLE INFO

Keywords:
Racecadotril
FMO
MEP
SARS-CoV-2
SMAD
Molecular docking

ABSTRACT

Racecadotril (RCL), a sulfur-containing compound, was analyzed through theoretical and experimental techniques to explore its structural, spectroscopic, electronic, and biological properties. C–H bonds primarily contribute to bond distances, while C–C–H angles are the most dominant among bond angles. The impact of solvent polarity on the Frontier Molecular Orbitals (FMO), electronic spectra, and Molecular Electrostatic Potential (MEP) mapping was examined, with a focus on polar solvents such as DMSO, ethanol, methanol, and water, as well as non-polar solvents like cyclohexane, toluene, and chloroform. Vibrational spectra exhibited characteristic bands associated with CH_3, CH_2, CH, NH, CC, CO, and CS stretching and deformation modes. Excitation wavelengths were identified in polar solvents at approximately 253 nm, 231 nm, and 229 nm, with corresponding wavenumbers ranging from 39496 cm^{-1} to 43647 cm^{-1}. In contrast, non-polar solvents caused a slight red shift, with wavenumbers ranging from 39241 cm^{-1} to 43605 cm^{-1}, indicating solvent-dependent electronic transitions. Lone pair interactions played a crucial role in molecular stabilization, with nitrogen-to-oxygen charge transfer contributing 49.21 kJ/mol, oxygen-to-oxygen at 48.04 kJ/mol, and carbon-carbon delocalization within a conjugated system at 21.45 kJ/mol. Mulliken charge analysis and MEP mapping further confirmed the presence of nucleophilic nitrogen and oxygen, electrophilic carbonyl carbons, and electron-withdrawing sulfur, with H33 exhibiting the highest electrophilicity due to nitrogen polarization. A topological study identified localized, delocalized, and weak interactions, shedding light on its electronic characteristics. Furthermore, molecular docking conducted against SARS-CoV-2 main proteases, spike glycoprotein, and oncoproteins from the SMAD family demonstrated the RCL's potential antiviral and antiproliferative activity.

1. Introduction

Over the past decades, sulfur-containing heterocyclic compounds have demonstrated significant biological applications and have been consistently utilized in the food and pharmaceutical industries [1,2]. Sulfur-containing phytocompounds, which are essential constituents of brassica vegetables, are highly reactive and volatile, and are used as flavoring agents in the food industry [3,4]. Additionally, sulfur-containing amino acids like cysteine and methionine are crucial for maintaining the stability of three-dimensional structures of proteins through disulfide bonds. Sulfur-containing drugs exhibit notable bioactive properties, including antiproliferative, antimicrobial, antidepressant, antiplatelet, and antidiabetic activities [5–10]. Racecadotril (RCL), chemically known as acetorphan or benzyl 2-(-3

---

* Corresponding author.
** Corresponding author.
E-mail addresses: cpavithra@mkjc.in (C. Pavithra), sselvaphy@gmail.com (S. Selvaraj).

https://doi.org/10.1016/j.jics.2025.101702
Received 11 November 2024; Received in revised form 26 March 2025; Accepted 4 April 2025

(acetylthio)-2-benzylpropanamido) acetate, is a sulfur-containing molecule with the chemical formula of $C_{21}H_{23}NO_4S$ and a molecular weight of 385.48 g/mol. RCL exists as two stereoisomers (R and S isomers) due to the spatial arrangement around the chiral center, known as ecadotril and retorphan [11]. As a prodrug, RCL acts as a specific enkephalinase inhibitor and is converted to the active form thiorphan upon oral administration. It is prescribed for treating acute diarrhea in both adults and children [12]. Furthermore, the concentration of thiorphan, the active metabolite, in human plasma has been determined using HPLC and LC methods [13,14].

SARS-CoV, a single-stranded RNA betacoronavirus with a 29.7 kb genome, triggered a global outbreak in 2003, resulting in around 800 fatalities worldwide. Similarly, the SARS-CoV-2 outbreak in 2019 escalated into a global pandemic, affecting more than 600 million people. The virus spread mainly through respiratory droplets from coughing and sneezing [15,16] and exhibited 96 % genetic similarity to bat coronavirus, while sharing approximately 80 % similarity with SARS-CoV and 50 % with MERS-CoV [17,18]. The main proteases (M^{pro}) of these viruses are essential for viral translation and replication, making them key targets for antiviral drug development. Several FDA-approved drugs has been designed to inhibit or block the activity of these main proteases [19]. In 2021, Chiou and colleagues examined a collection of 774 FDA-approved compounds for their potential to act as antagonists against the SARS-CoV-2 M^{pro} protein [20]. However, as of now, no definitive therapeutic solutions for SARS-CoV-2 treatment have been developed.

Density Functional Theory (DFT) has become an essential tool in drug discovery, known for its computational precision and ability to predict the behavior of both natural and synthesized compounds as repoted in the literature [21–23]. This approach has significantly advanced our ability to design and evaluate new drugs by providing detailed insights into their molecular behavior. Several sulfur-containing FDA-approved drugs, including pioglitazone, clopidogrel, olanzapine, famotidine, and febuxostat, have been characterized using theoretical and experimental spectroscopic methods [24–28]. However, there is a notable lack of spectroscopic characterization for RCL in the existing literature. This gap highlights the need to prioritize RCL in our research efforts. The present work aims to comprehensively investigate the spectroscopic, structural, biological, electronic, and topological properies of RCL through both theoretical and experimental methods.

2. Materials and methods

2.1. Sample and experimental procedures

A high-purity sample of RCL was procured from Sigma Aldrich Co., USA, and was used directly in experimental studies without any further processing. The FT-IR spectrum was recorded using an Alpha-Platinum-ATR-IR module in combination with a Rock-Solid Michelson Interferometer (Bruker), while the FT-Raman spectrum was recorded using an Imaging Spectrograph STR 500 mm Focal Length Laser Raman spectrometer (Technos Instruments). The UV–Vis spectrum was measured using a UV-DRS Spectrophotometer (Thermo Fisher).

2.2. Computational methodologies

All computational calculations were conducted using the DFT/B3LYP/6-31G(d,p) basis set within the Gaussian 16W program package [29–35]. Time-Dependent Density Functional Theory (TD-DFT) calculations were conducted with the same basis set to evaluate electronic properties [36–38]. The Density of States (DOS) in different solvents (polar and non-polar) was determined using the GaussSum program [39]. Data visualization was carried out using GaussView 6 [40] and Chemcraft software [41]. For Natural Bond Orbital (NBO) analysis, NBO Version 3.1 [42], integrated into the Gaussian package, was utilized. Structural and binding analyses of ligand-protein complexes were conducted using the PyMOL software [43], while AutoDock [44] was employed to predict ligand-receptor binding affinities. Topological evaluations, including Electron Localization Function (ELF), Local Orbital Locator (LOL), Reduced Density Gradient (RDG), and Non-Covalent Interactions (NCI), were carried out using the Atomistica online molecular modeling platform and Multiwfn software [45–47], with visualizations generated using the VMD program [48].

3. Results and discussion

3.1. Optimized geometry

The optimized geometrical parameters for RCL are outlined in Table 1 and illustrated in Fig. 1. The optimized structure of RCL consists of 51 bond distances and 86 bond angles, including 19 C–C bonds, 2 S–C and N–C bonds, 5 O–C bonds, 1 N–H bond, and 22 C–H bond distances. Similarly, the structure features 19 C–C–C bond angles and one instance of each of O–C–N, S–C–O, C–S–C, C–O–C, O–C–O, and C–N–C bond angles. Additionally, it includes two instances of S–C–H, N–C–C, C–N–H, O–C–H, S–C–C, and N–C–H bond angles, 37 C–C–H bond angles, 7 H–C–H bond angles, and 5 O–C–C bond angles.

The bond distances of S_1–C_9 and S_1–C_{19} in the acetylthio group were calculated to be 1.836 and 1.804 Å, respectively. The RCL structure encompasses three double-bonded oxygen atoms (O_2, O_4, and O_5) stem from carbon atoms C_{11}, C_{18}, and C_{19}, forming $O_2{=}C_{11}$, $O_4{=}C_{18}$, and $O_5{=}C_{19}$ with bond distances of 1.227 Å, 1.210 Å, and 1.213 Å, respectively. Single-bonded O_3–C_{18} and O_3–C_{20} distances were calculated to be 1.480 Å and 1.455 Å. In the benzyl propenamide structure, the bond distances of N_6–H_{33}, N_6–C_{11}, and N_6–C_{14} were found to be 1.009 Å, 1.369 Å, and 1.448 Å, respectively. The bond distances of C–H and C–C in the benzyl structure ranged between 1.086 and 1.087 Å and 1.393–1.403 Å. The bond distances of C_{22}–H_{43}, C_{22}–H_{44}, and C_{22}–H_{45} in the methyl group of the acetylthio group were calculated as 1.095 Å, 1.092 Å, and 1.093 Å. Conversely, the bond distances of C–H in the CH_2 groups ranged between 1.093 and 1.095 Å. The bond distances of C–C in the chain structure varied between 1.504 and 1.547 Å.

The bond angles of C–C–H and C–C–C in the benzyl structure were found to be between 119.3-120.4° and 118.4–120.5°, respectively. The bond angles of C_9–S_1–C_{19}, S_1–C_{19}–O_5, S–C–C, and S–C–H were measured at 99.90°, 123.8°, 113.2°–116.2°, and 104.8°–106.6°, respectively. The bond angles of $O_2{=}C_{11}$–C_7, $O_4{=}C_{18}$–C_{14}, and $O_5{=}C_{19}$–C_{22} were 122.3°, 123.4°, and 123.1°, respectively. In contrast, the bond angles of O_3–C_{18}–C_{14} and O_3–C_{20}–C_{21} were 112° and 108.1°, respectively. The bond angles involving double-bonded oxygen atoms are larger compared to those single-bonded oxygen atoms due to sp^2 and sp^3 hybridizations. The bond angles of O_2–C_{11}–N_6, C_{18}–O_3–C_{20}, O_3–C_{18}–O_4, and O–C–H were 122.6°, 116°, 124.5°, and 107.8°–108.9°, respectively. The bond angles of H–C–H in methylene (CH_2) and methyl (CH_3) groups ranged from 107° to 108.9° and 107.8°–110.1°, respectively. The C_{11}–N_6–C_{14}, C–N–H, N–C–H and N–C–C bond angles were simulated within 121.4°, 117.2°–118.7°, 107.7°–111.6°, and 111.6°–115°, respectively. Similarly, the bond angles of C–C–C and C–C–H were simulated between 110.3° to 121.1° and 105.2°–112.7°, respectively.

3.2. Vibrational properties

The RCL compound, consisting of 50 atoms, exhibits 144 vibrational modes, adhering to the (3N-6) rule and C_1 point group symmetry. The theoretical vibrational spectra were generated using Chemcraft software, employing a Lorentzian line shape together with a full width at half maximum (FWHM) of 54 cm^{-1}. Experimentally observed vibrational frequencies were found to be slightly higher than theoretical predictions due to anharmonicity in real systems. To mitigate this discrepancy, the computed wavenumbers were scaled by a factor of 0.96, which is standard practice in computational chemistry. A

Table 1
Optimized geometrical parameters of RCL.

Bond lengths (Å)	Theoretical	Bond lengths (Å)	Theoretical	Bond lengths (Å)	Theoretical
S_1–C_9	1.836	C_9–H_{31}	1.093	C_{20}–C_{21}	1.504
S_1–C_{19}	1.804	C_9–H_{32}	1.094	C_{20}–H_{41}	1.094
O_2–C_{11}	1.227	C_{10}–C_{12}	1.402	C_{20}–H_{42}	1.094
O_3–C_{18}	1.348	C_{10}–C_{13}	1.403	C_{21}–C_{23}	1.398
O_3–C_{20}	1.455	C_{12}–C_{15}	1.396	C_{21}–C_{24}	1.402
O_4–C_{18}	1.210	C_{12}–H_{34}	1.088	C_{22}–H_{43}	1.095
O_5–C_{19}	1.213	C_{13}–C_{16}	1.396	C_{22}–H_{44}	1.092
N_6–C_{11}	1.369	C_{13}–H_{35}	1.086	C_{22}–H_{45}	1.093
N_6–C_{14}	1.448	C_{14}–C_{18}	1.524	C_{23}–C_{25}	1.396
N_6–H_{33}	1.009	C_{14}–H_{36}	1.098	C_{23}–H_{46}	1.087
C_7–C_8	1.545	C_{14}–H_{37}	1.092	C_{24}–C_{26}	1.393
C_7–C_9	1.547	C_{15}–C_{17}	1.396	C_{24}–H_{47}	1.086
C_7–C_{11}	1.534	C_{15}–H_{38}	1.087	C_{25}–C_{27}	1.395
C_7–H_{28}	1.099	C_{16}–C_{17}	1.397	C_{25}–H_{48}	1.086
C_8–C_{10}	1.515	C_{16}–H_{39}	1.086	C_{26}–C_{27}	1.398
C_8–H_{29}	1.093	C_{17}–H_{40}	1.086	C_{26}–H_{49}	1.086
C_8–H_{30}	1.095	C_{19}–C_{22}	1.515	C_{27}–H_{50}	1.086
Bond angles (○)	**Theoretical**	**Bond angles (○)**	**Theoretical**	**Bond angles (○)**	**Theoretical**
C_9–S_1–C_{19}	99.90	C_9–C_7–C_{11}	110.3	C_{16}–C_{17}–H_{40}	120.3
S_1–C_9–C_7	116.2	C_9–C_7–H_{28}	105.2	C_{19}–C_{22}–H_{43}	108.4
S_1–C_9–H_{31}	106.6	C_7–C_9–H_{31}	110.3	C_{19}–C_{22}–H_{44}	112.7
S_1–C_9–H_{32}	104.8	C_7–C_9–H_{32}	109.7	C_{19}–C_{22}–H_{45}	108.8
S_1–C_{19}–O_5	123.8	C_{11}–C_7–H_{28}	108.7	C_{21}–C_{20}–H_{41}	112.4
S_1–C_{19}–C_{22}	113.2	C_{10}–C_8–H_{29}	110.2	C_{21}–C_{20}–H_{42}	112.0
O_2–C_{11}–N_6	122.6	C_{10}–C_8–H_{30}	109.7	C_{20}–C_{21}–C_{23}	120.5
O_2–C_{11}–C_7	122.3	C_8–C_{10}–C_{12}	120.5	C_{20}–C_{21}–C_{24}	120.3
C_{18}–O_3–C_{20}	116.0	C_8–C_{10}–C_{13}	121.1	H_{41}–C_{20}–H_{42}	107.6
O_3–C_{18}–O_4	124.5	H_{29}–C_8–H_{30}	107.6	C_{23}–C_{21}–C_{24}	119.2
O_3–C_{18}–C_{14}	112.0	H_{31}–C_9–H_{32}	108.9	C_{21}–C_{23}–C_{25}	120.5
O_3–C_{20}–C_{21}	108.1	C_{12}–C_{10}–C_{13}	118.4	C_{21}–C_{23}–H_{46}	119.6
O_3–C_{20}–H_{41}	107.8	C_{10}–C_{12}–C_{15}	121.0	C_{21}–C_{24}–C_{26}	120.3
O_3–C_{20}–H_{42}	108.9	C_{10}–C_{12}–H_{34}	119.3	C_{21}–C_{24}–H_{47}	119.9
O_4–C_{18}–C_{14}	123.4	C_{10}–C_{13}–C_{16}	120.7	H_{43}–C_{22}–H_{44}	108.9
O_5–C_{19}–C_{22}	123.1	C_{10}–C_{13}–H_{35}	119.1	H_{43}–C_{22}–H_{45}	107.8
C_{11}–N_6–C_{14}	121.4	C_{15}–C_{12}–H_{34}	119.6	H_{44}–C_{22}–H_{45}	110.1
C_{11}–N_6–H_{33}	118.7	C_{12}–C_{15}–C_{17}	120.1	C_{25}–C_{23}–H_{46}	119.8
N_6–C_{11}–C_7	115.0	C_{12}–C_{15}–H_{38}	119.8	C_{23}–C_{25}–C_{27}	120.0
C_{14}–N_6–H_{33}	117.2	C_{16}–C_{13}–H_{35}	120.2	C_{23}–C_{25}–H_{48}	119.8
N_6–C_{14}–C_{18}	114.9	C_{13}–C_{16}–C_{17}	120.3	C_{26}–C_{24}–H_{47}	119.8
N_6–C_{14}–H_{36}	111.6	C_{13}–C_{16}–H_{39}	119.7	C_{24}–C_{26}–C_{27}	120.2
N_6–C_{14}–H_{37}	107.7	C_{18}–C_{14}–H_{36}	106.8	C_{24}–C_{26}–H_{49}	119.4
C_8–C_7–C_9	112.8	C_{18}–C_{14}–H_{37}	108.5	C_{27}–C_{25}–H_{48}	120.2
C_8–C_7–C_{11}	111.1	H_{36}–C_{14}–H_{37}	107.0	C_{25}–C_{27}–C_{26}	119.8
C_8–C_7–H_{28}	108.5	C_{17}–C_{15}–H_{38}	120.1	C_{25}–C_{27}–H_{50}	120.1
C_7–C_8–C_{10}	113.5	C_{15}–C_{17}–C_{16}	119.5	C_{27}–C_{26}–H_{49}	120.4
C_7–C_8–H_{29}	107.6	C_{15}–C_{17}–H_{40}	120.3	C_{26}–C_{27}–H_{50}	120.1
C_7–C_8–H_{30}	108.1	C_{17}–C_{16}–H_{39}	120.0	–	–

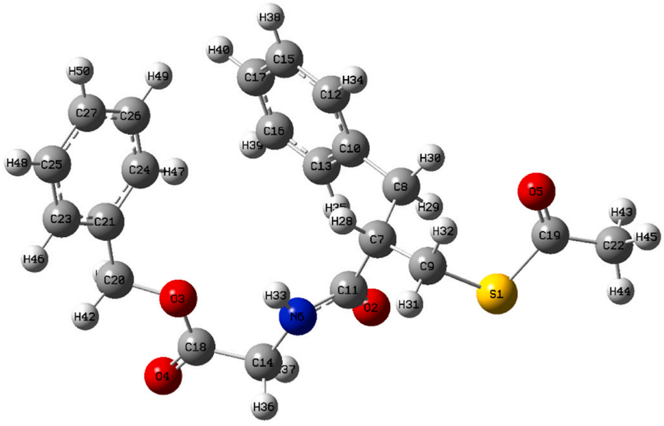

Fig. 1. Optimized molecular structure of RCL.

comparison of theoretical and experimental vibrational wavenumbers is presented in Table 2, with the corresponding spectra depicted in Figs. 2 and 3. The vibrational spectra reveal prominent peaks corresponding to CH_3, CH_2, CH, NH, CO, CC, and CS stretching and deformation modes.

The electronic structure of RCL includes a single methyl (CH_3) group, which gives rise to asymmetric and symmetric stretching modes. Literature values place these bands at 2980 cm^{-1} and 2870 cm^{-1}, respectively [49]. For RCL, a single symmetric band was theoretically predicted at 2937 cm^{-1} and experimentally recorded at 2938 cm^{-1} (FT-Raman). The asymmetric stretching bands were computed at 3032 cm^{-1} and 3008 cm^{-1} and observed at 3031 cm^{-1} (FT-IR). The C–S stretching modes arise due to the sulfur atom's linkage with carbonyl (C=O) and methylene (CH_2) groups. Typically, these vibrations occur between 730 and 660 cm^{-1}. For RCL, the C–S stretching bands were simulated at 681 cm^{-1} and 614 cm^{-1}, while experimental measurements recorded them at 626 cm^{-1} (FT-IR) and 621 cm^{-1} (FT-Raman). The C=O (carbonyl) stretching vibrations result from the oxygen atoms bonded to carbon via double bonds. Theoretically, these modes were identified at 1759 cm^{-1} (C18–O4), 1714 cm^{-1} (C19–O5), and 1697 cm^{-1} (C11–O2). Experimentally, corresponding bands were observed at 1727 cm^{-1} and 1685 cm^{-1} (FT-IR) and 1726 cm^{-1} (FT-Raman). The CH_2

Table 2
Experimental (FT-IR and FT-Raman) and theoretical wavenumbers (cm^{-1}) and vibrational assignments of RCL.

Modes	Experimental wavenumbers (cm^{-1})		Theoretical wave numbers (cm^{-1})				Vibrational assignments
	FT-IR	FT-Raman	Unscaled	Scaled	I_{IR}	I_{Raman}	
1.	–	–	3644	3498	38.51	41.14	υ NH
2.	3282, 3087	3290	3209	3081	12.19	322.94	υ CH
3.	–	–	3206	3078	10.33	179.91	υ CH
4.	–	–	3200	3072	23.14	35.42	υ CH
5.	–	–	3198	3070	19.95	69.95	υ CH
6.	–	–	3192	3064	12.07	120.17	υ CH
7.	3061	–	3187	3060	21.79	64.03	υ CH
8.	–	3058	3184	3057	2.99	76.09	υ CH
9.	–	–	3178	3051	0.86	81.14	υ CH
10.	–	–	3175	3048	4.81	47.04	υ CH
11.	–	–	3168	3041	6.24	34.66	υ CH
12.	3031	–	3158	3032	5.53	69.06	υ$_{as}$ CH$_3$
13.	–	–	3134	3009	9.44	42.80	υ$_{as}$ CH$_2$
14.	–	–	3133	3008	4.28	88.41	υ$_{as}$ CH$_3$
15.	–	–	3132	3007	4.79	45.52	υ$_{as}$ CH$_2$
16.	–	–	3122	2997	2.74	21.26	υ$_{as}$ CH$_2$
17.	–	2990	3117	2992	13.22	41.42	υ$_{as}$ CH$_2$
18.	–	–	3072	2949	14.83	94.95	υ$_{s}$ CH$_2$
19.	–	–	3069	2946	14.62	85.78	υ$_{s}$ CH$_2$
20.	–	–	3067	2944	17.59	55.51	υ$_{s}$ CH$_2$
21.	–	2938	3059	2937	1.24	178.90	υ$_{s}$ CH$_3$
22.	2917	–	3040	2918	29.43	151.08	υ$_{s}$ CH$_2$
23.	2898, 2850	2840	3024	2903	17.57	61.44	υ CH
24.	–	–	1832	1759	287.04	5.52	υ C=O
25.	1727	1726	1785	1714	190.12	3.56	υ C=O
26.	1685	–	1768	1697	153.10	13.40	υ C=O, δ NH
27.	1643	1604	1665	1598	0.38	34.87	υ CC, β CH
28.	1603	–	1661	1595	7.61	32.92	υ CC, β CH
29.	–	1565	1644	1578	0.47	6.72	υ CC, β CH, τ CH$_2$
30.	1549	1534	1637	1572	1.60	6.79	υ CC, β CH, τ CH$_2$
31.	1497	–	1544	1482	259.85	1.70	δ NH, τ CH$_2$
32.	–	–	1543	1481	8.03	1.78	υ CC, δ CH, δ NH
33.	–	–	1539	1477	24.75	0.27	β CH, δ NH
34.	1455	–	1514	1453	4.74	8.51	χ CH$_2$
35.	–	–	1503	1443	6.72	5.70	χ CH$_2$
36.	–	–	1496	1436	10.54	0.58	β CH, ρ CH$_2$
37.	–	–	1495	1435	5.71	1.11	β CH, ρ CH$_2$
38.	1426	1428	1488	1428	11.49	19.74	δ$_s$ CH$_3$
39.	–	–	1484	1425	7.07	11.89	χ CH$_2$
40.	–	–	1480	1421	7.29	15.11	δ$_s$ CH$_3$
41.	1401	–	1474	1415	13.22	19.00	χ CH$_2$
42.	1378	1381	1414	1357	7.61	16.94	β CH, ω CH$_2$
43.	–	1377	1407	1351	1.76	5.95	ω CH$_2$, β CH, δ NH
44.	1343	1349	1399	1343	16.46	9.24	δ$_{as}$ CH$_3$
45.	–	–	1371	1316	3.89	22.65	β CH, ω CH$_2$
46.	–	–	1366	1311	0.31	0.28	β CH, ω CH$_2$
47.	–	–	1364	1309	2.04	0.88	β CH
48.	–	–	1361	1307	0.80	2.99	β CH, ω CH$_2$
49.	–	–	1354	1300	0.78	1.20	β CH, ω CH$_2$
50.	1290	–	1350	1296	1.95	2.72	β CH, ω CH$_2$
51.	1248	1261	1329	1276	20.07	7.80	β CH, ω CH$_2$
52.	1235	1221	1281	1230	419.88	5.07	τ CH$_2$, δ NH, δ C=O
53.	1221	–	1259	1209	3.02	11.67	τ CH$_2$, δ NH, β CH
54.	–	–	1256	1206	26.98	5.12	τ CH$_2$
55.	1202	–	1252	1202	145.48	4.86	τ CH$_2$, β CH
56.	–	–	1243	1193	0.79	9.33	τ CH$_2$, β CH
57.	–	1189	1237	1188	3.53	24.94	τ CH$_2$, β CH
58.	–	1181	1230	1181	36.34	9.79	τ CH$_2$, δ NH, β CH
59.	–	–	1228	1179	51.02	3.83	ω CH$_2$, β CH, δ NH,
60.	–	–	1210	1162	0.92	6.71	β CH
61.	–	–	1208	1160	0.47	14.70	β CH
62.	–	–	1196	1148	35.64	8.09	τ CH$_2$, δ NH, β CH
63.	–	–	1187	1140	0.36	9.71	β CH
64.	1133	–	1186	1139	0.29	4.54	β CH
65.	1099		1136	1091	212.12	0.80	δ C=O, δ$_{as}$ CH$_3$
66.	1081	–	1127	1082	3.60	2.92	τ CH$_2$, δ NH, β CH
67.	–	–	1117	1072	2.48	1.19	β CH, ρ CH$_2$
68.	1055	–	1108	1064	7.25	1.42	β CH
69.	1028	1034	1072	1029	7.27	4.50	τ CH$_2$, δ NH, β CH
70.	1017	–	1056	1014	5.87	6.49	β CH
71.	–	–	1055	1013	0.36	15.31	β CH
72.	–	1001	1053	1011	6.40	4.60	τ CH$_2$, δ NH, β CH
73.	980	–	1024	983	8.22	1.70	δ$_{as}$ CH$_3$

(*continued on next page*)

Table 2 (*continued*)

Modes	Experimental wavenumbers (cm^{-1})		Theoretical wave numbers (cm^{-1})				Vibrational assignments
	FT-IR	FT-Raman	Unscaled	Scaled	I_{IR}	I_{Raman}	
74.	–	–	1018	977	1.01	17.99	γ CH, ρ CH_2
75.	–	–	1016	975	1.52	29.30	γ CH
76.	–	–	1013	972	52.94	4.11	ρ CH_2, δ NH, γ CH, δ_{as} CH_3
77.	–	–	1007	967	7.37	2.67	γ CH, ρ CH_2
78.	960	–	1001	961	43.82	3.70	γ CH, ρ CH_2
79.	–	–	1000	960	40.92	6.73	γ CH, ρ CH_2
80.	–	–	999	959	3.57	0.73	γ CH, ρ CH_2
81.	–	–	985	946	48.44	4.57	γ CH, ρ CH_2, δ_{as} CH_3
82.	940	–	981	942	2.03	0.11	γ CH
83.	–	934	978	939	0.12	0.27	γ CH
84.	–	–	965	926	6.37	6.13	γ CH, ρ CH_2
85.	912	–	945	907	18.16	17.04	γ CH, ρ CH_2
86.	899	897	931	894	3.33	1.12	γ CH
87.	875	–	924	887	9.01	7.73	γ CH
88.	855	851	890	854	0.62	2.64	ρ CH_2
89.	–	–	880	845	4.76	3.76	ρ CH_2, δ NH, γ CH
90.	–	830	869	834	0.60	3.01	γ CH
91.	820	–	865	830	0.07	4.52	γ CH
92.	803	–	841	807	0.82	4.19	ρ CH_2, γ CH
93.	–	–	826	793	2.78	5.90	ρ CH_2, γ CH
94.	750	749	773	742	34.35	1.65	γ CH
95.	–	–	766	735	26.17	4.81	γ CH
96.	719	–	765	734	15.09	2.92	γ CH, δ C=O
97.	694	711	720	691	26.86	1.15	γ CH
98.	–	–	714	685	16.72	0.99	γ CH
99.	–	–	709	681	2.81	6.87	δ C=O, ρ CH_2, δ NH, υ CS
100.	–	–	667	640	11.34	1.36	ω CH_2, δ NH
101.	626	621	640	614	1.98	1.98	δ C=O, ρ CH_2, δ NH, υ CS
102.	–	–	636	611	0.21	3.45	δ CH
103.	–	–	632	606	0.23	5.03	, δ NH
104.	597	–	617	592	70.80	19.50	δ C=O, δ_{as} CH_3
105.	–	–	605	581	10.10	1.90	δ CH, δ C=O, ρ CH_2, δ NH
106.	578	–	603	579	6.29	1.75	δ CH, δ C=O, ρ CH_2, δ NH
107.	553	–	581	557	6.04	1.22	δ CH, δ C=O, ρ CH_2, δ NH
108.	–	–	569	546	5.14	1.54	δ CH, δ C=O, ρ CH_2, δ NH
109.	529	530	535	514	1.03	2.11	δ C=O, δ_{as} CH_3
110.	507	–	517	496	62.3	1.62	δ NH
111.	–	–	508	488	40.13	0.57	δ NH, δ CH
112.	–	–	493	473	9.11	3.26	δ CH, δ C=O, ρ CH_2, δ NH
113.	–	–	489	469	3.19	2.86	δ CH, δ C=O, ρ CH_2, δ NH
114.	–	–	442	424	12.28	1.40	δ CH, δ C=O, ρ CH_2, δ NH
115.	–	–	420	403	0.24	0.17	δ CH
116.	–	–	416	399	0.53	0.15	δ CH
117.	–	–	389	373	8.81	0.53	δ CH, ρ CH_2, δ NH
118.	–	–	373	358	6.39	1.05	δ_{as} CH_3, ρ CH_2, δ NH, δ CH
119.	–	–	356	342	8.85	1.62	δ_{as} CH_3, ρ CH_2, δ NH, δ CH
120.	–	–	348	334	3.92	0.53	δ_{as} CH_3, ρ CH_2, δ NH, δ CH
121.	–	–	296	284	8.02	0.98	ρ CH_2, δ NH, δ CH
122.	–	–	294	282	15.02	1.02	δ CH, δ C=O, ρ CH_2, δ NH
123.	–	–	282	271	1.98	0.60	δ CH, ρ CH_2
124.	–	–	244	234	4.04	2.75	δ CH, δ C=O, δ NH
125.	–	–	226	217	3.31	4.02	δ CH, δ C=O, ρ CH_2, δ NH
126.	–	–	195	187	1.43	1.19	δ CH, δ C=O, ρ CH_2, δ NH
127.	–	–	189	181	2.69	2.36	δ CH, δ C=O, ρ CH_2, δ NH
128.	–	–	157	151	1.10	1.14	δ CH, δ C=O, ρ CH_2, δ NH
129.	–	–	150	144	1.96	0.64	δ CH, ρ CH_2
130.	–	–	127	122	3.66	1.98	δ CH, δ C=O, ρ CH_2, δ NH
131.	–	–	95	91	7.06	1.32	δ C=O, δ_{as} CH_3
132.	–	–	94	90	2.75	3.06	δ C=O, δ_{as} CH_3
133.	–	–	70	67	3.41	2.75	δ CH, δ C=O, ρ CH_2, δ NH, δ_{as} CH_3
134	–	–	59	57	1.58	2.71	δ_{as} CH_3, δ CH
135.	–	–	51	49	0.98	3.83	δ CH, δ C=O, ρ CH_2, δ NH, δ_{as} CH_3
136.	–	–	41	39	1.77	0.44	δ C=O, δ_{as} CH_3
137.	–	–	37	36	0.33	5.08	δ CH
138.	–	–	36	35	2.34	0.25	δ C=O, δ_{as} CH_3
139.	–	–	32	31	0.52	1.96	δ_{as} CH_3
140.	–	–	30	29	0.20	4.86	δ C=O, δ_{as} CH_3
141.	–	–	26	25	0.07	4.62	δ C=O, δ_{as} CH_3
142.	–	–	23	22	0.53	1.14	δ C=O, δ_{as} CH_3
143.	–	–	17	16	0.27	3.79	Ring vibration
144.	–	–	11	10	0.47	2.52	Ring vibration

υ_s - symmetric stretching; υ_{as} - asymmetric stretching; δ - bending/deformation; β – in-plane bending; γ – out-of-plane bending; χ - scissoring; ω - wagging; τ - twist; ρ – rocking, Scaling factor 0.96 for all vibrations.

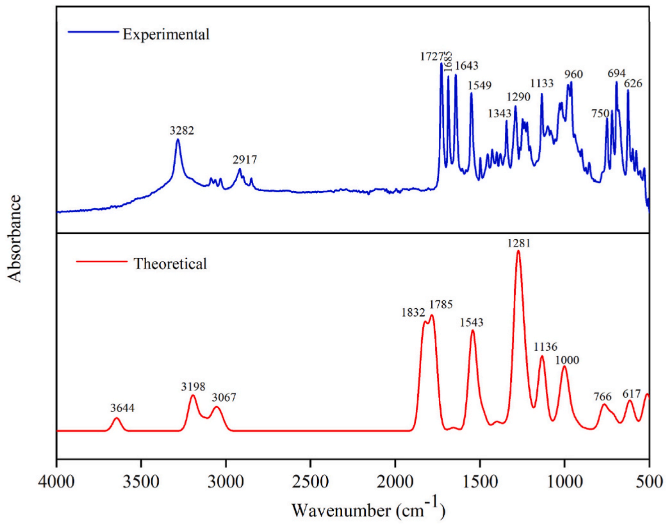

Fig. 2. Theoretical and experimental FT-IR spectra of RCL.

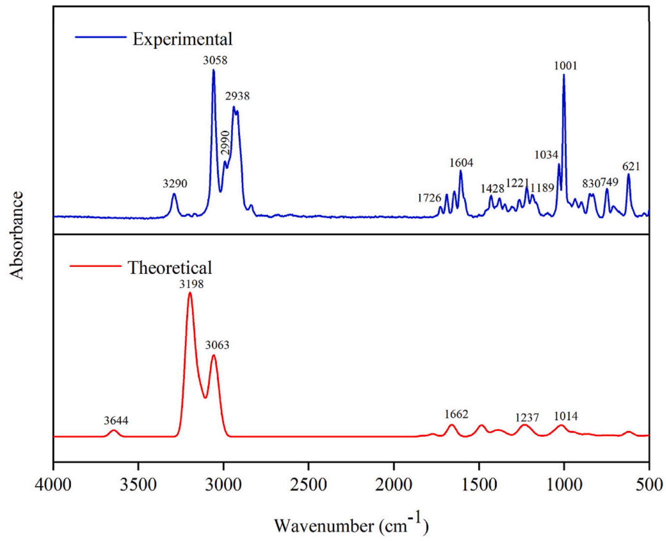

Fig. 3. Theoretical and experimental FT-Raman spectra of RCL.

symmetric and asymmetric modes are reported to span between 3000-2900 and 3000-3100 cm^{-1} [50]. In this finding, the asymmetric CH_2 modes were simulated at 3009, 3007, 2997, and 2992 cm^{-1} for C_{14}–$H_{36,37}$, C_9–$H_{31,32}$, C_8–$H_{29,30}$, and C_{20}–$H_{41,42}$, respectively, and recorded at 2990 cm^{-1} in the FT-Raman spectrum. Similarly, the symmetric CH_2 stretching was calculated at 2949, 2946, 2944, and 2918 cm^{-1}, with experimental peak at 2917 cm^{-1} (FT-IR). In the literature, the CH bands are characteristic modes in the heteroaromatic structure spanning 3100-3000 cm^{-1} [51–54]. In RCL, these modes were computed between 3081 and 3041 cm^{-1} region, and were experimentally observed at 3282, 3087, 3061 cm^{-1} (FT-IR) and 3290, 3058 cm^{-1} (FT- Raman). For sulfonamide derivatives, literature suggests N–H stretching bands occur around 3474, 3372, and 3379 cm^{-1} [55,56]. In line with this observation, the N_6–H_{33} stretching mode was theoretically predicted to be 3498 cm^{-1}.

The vibrational modes for symmetric and asymmetric deformations of CH_3 are reported to span between 1465-1440 and 1390-1370 cm^{-1} [57]. In RCL, these symmetric and asymmetric deformation modes were simulated at 1428, 1421, and 1343 cm^{-1} and observed at 1426 cm^{-1} (FT-IR), 1428 cm^{-1} (FT-Raman), 1343 cm^{-1} (FT-IR), and 1349 cm^{-1} (FT-Raman). Similarly, the methylene (CH_2) deformations, such as rocking, wagging, twisting, and scissoring were observed below 1500 cm^{-1} for RCL. The C–H deformations are typically observed within the ranges of 1450-1000 cm^{-1} for in-plane deformations and 1000-750 cm^{-1} for out-of-plane deformations [58]. Theoretical calculations for RCL estimated in-plane deformations within 1598-1011 cm^{-1}, while out-of-plane deformations ranged from 977 to 685 cm^{-1}. Experimental results showed in-plane modes at 1643-1017 cm^{-1} (FT-IR) and 1604-1001 cm^{-1} (FT-Raman), while out-of-plane modes appeared at 960-694 cm^{-1} (FT-IR) and 934-711 cm^{-1} (FT-Raman).

3.3. *Influence of solvents on electronic properties*

3.3.1. *Electronic spectra*

The calculated electronic spectral properties of RCL in different solvent environments, both polar and non-polar, are summarized in Table 3, and visualized in Fig. 4, while the experimental spectrum in ethanol is presented in Fig. 5. In polar solvents like dimethyl sulfoxide (DMSO), ethanol, methanol, and water, the excitation wavelengths are approximately 253 nm, 231 nm, and 229 nm, with corresponding wavenumbers ranging from 39496 cm^{-1} to 43647 cm^{-1}. The oscillator strengths in these cases are generally low, indicating weak electronic transitions. The major contributors to these transitions involve transitions from the Highest Occupied Molecular Orbital (HOMO) to the Lowest Unoccupied Molecular Orbital (LUMO) and other nearby orbitals. For instance, in DMSO, the first excitation at 253.13 nm (4.898 eV, 39505 cm^{-1}) shows significant contributions from H-7→L (39 %) and H-6→L (50 %), with an oscillator strength of 0.0002. The second excitation at 230.63 nm (5.375 eV, 43359 cm^{-1}) shows a slight increase in oscillator strength of 0.0027, with H-2→L+4 (22 %) and H→L+2 (30 %) major contributions. Similarly, in ethanol, methanol, and water, these transitions were consistently significant. In contrast, for non-polar solvents like cyclohexane, toluene, and chloroform, the wavelengths are marginally red-shifted compared to those observed in polar solvents, with wavenumbers ranging from 39241 cm^{-1} to 43605 cm^{-1}. The oscillator strengths are slightly higher, suggesting stronger transitions in non-polar environments. For example, in chloroform, the first excitation at 253.89 nm (4.883 eV, 39387 cm^{-1}) shows significant contributions from H-7→L (41 %) and H-6→L (46 %), with an oscillator strength of 0.0002. The second excitation at 230.74 nm (5.373 eV, 43338 cm^{-1}) has an oscillator strength of 0.0027, with H→L+3 (46 %) and H-1→L+4 (21 %) contributions. Similar trends were observed in cyclohexane and toluene, where the H-7→L and H-6→L transitions remained significant.

Experimentally, a prominent peak was observed at 306 nm, which appears to be red-shifted compared to the theoretical predictions. The calculated excitation energies (E) and wavenumbers provide insight into the energy levels and transitions within the molecule. For instance, the excitation energies for the peak at 253 nm were approximately 4.89 eV across all solvents, indicating a stable electronic excitation behavior. The oscillator strengths, though relatively low, suggest that the transitions are allowed but not highly probable, consistent with the nature of π→π* or n→π* transitions typically observed in Ultraviolet–Visible (UV–Vis) spectroscopy. Notably, while there are variations in wavenumbers due to differing solvent environments, the overall excitation wavelengths, energies, oscillator strengths, and major contributions remain remarkably consistent across both polar and non-polar solvents. This uniformity suggests that the electronic structure of RCL is resilient and not substantially affected by the surrounding solvent environment, thus maintaining consistent excitation properties. The variations in wavenumbers are primarily attributed to the differing solvent polarities, which can slightly affect the energy levels but not enough to cause substantial changes in other properties.

3.3.2. *Reactivity, stability and molecular orbitals*

In computational chemistry, the Frontier Molecular Orbitals (FMO) are essential for assessing the stability and chemical reactivity of molecular structures [59]. Figs. S1 and S2 (Supplementary Material)

Table 3
Calculated wavelengths (λ), excitation energies (E), oscillator strengths (f), and major contributions of RCL in various solvent.

Solvents	λ (nm)	Wavenumber (cm^{-1})	E (eV)	f	Major contributions	Minor contributions
Polar Solvents						
DMSO	253.13	39505	4.898	0.0002	H-7→L (39 %) H-6→L (50 %)	H-5→L (9 %)
	230.63	43359	5.375	0.0027	H-2→L+4 (22 %) H→L+2 (30 %)	H→L+3 (16 %) H-2→L+2 (3 %) H-1→L+2 (2 %) H-1→L+4 (6 %) H→L+4 (4 %) H→L (8 %)
	229.15	43639	5.410	0.0019	H-4→L+1 (47 %) H-1→L+3 (20 %)	H-3→L+3 (2 %) H-3→L+1 (2 %) H-2→L+1 (2 %) H-2→L+2 (3 %) H-2→L+3 (7 %) H-1→L+2 (8 %)
Ethanol	253.19	39496	4.896	0.0002	H-7→L (39 %) H-6→L (49 %)	H-5→L (9 %)
	230.62	43361	5.376	0.0026	H-2→L+4 (20 %) H→L+2 (21 %)	H→L+3 (26 %) H-2→L+2 (2 %) H-1→L+2 (2 %) H-1→L+4 (8 %) H→L+4 (4 %) H→L (8 %)
	229.15	43639	5.410	0.0018	H-4→L+1 (48 %) H-1→L+3 (12 %)	H-1→L+3 (12 %) H-2→L+1 (2 %) H-2→L+2 (7 %) H-2→L+3 (6 %)
Methanol	253.14	39503	4.897	0.0002	H-7→L (39 %), H-6→L (50 %)	H-5→L (9 %)
	230.61	43363	5.376	0.0025	H-2→L+4 (21 %), H→L+2 (26 %)	H→L+3 (21 %) H-2→L+2 (3 %) H-1→L+2 (2 %) H-1→L+4 (7 %) H→L+4 (4 %) H→L (8 %)
	229.13	43643	5.411	0.0018	H-4→L+1 (48 %), H-1→L+3 (16 %)	H-1→L+3 (10 %) H-2→L+1 (2 %) H-2→L+2 (5 %) H-2→L+3 (7 %)
Water	253.07	39514	4.899	0.0002	H-7→L (39 %), H-6→L (50 %)	H-5→L (9 %)
	230.59	43367	5.376	0.0025	H-2→L+4 (23 %), H→L+2 (34 %)	H→L+3 (13 %) H-2→L+2 (3 %) H-1→L+2 (2 %) H-1→L+4 (5 %) H→L+4 (4 %) H→L (8 %)
	229.11	43647	5.411	0.0018	H-4→L+1 (47 %), H-1→L+3 (23 %)	H-1→L+3 (2 %) H-2→L+1 (3 %) H-2→L+2 (2 %) H-2→L+3 (2 %)
Non-polar solvents						
Chloroform	253.89	39387	4.883	0.0002	H-7→L (41 %), H-6→L (46 %)	H-5→L (11 %)
	230.74	43338	5.373	0.0027	H→L+3 (46 %), H-1→L+4 (21 %)	H-3→L+4 (2 %) H-2→L+4 (8 %) H-1→L+3 (4 %) H→L (7 %) H→L+4 (4 %)
	229.33	43605	5.460	0.0018	H-4→L+1 (50 %) H-2→L+2 (28 %)	H-5→L+2 (4 %) H-3→L+2 (6 %) H-1→L+2 (6 %)
Cyclohexane	254.83	39241	4.865	0.0002	H-7→L (41 %) H-6→L (43 %)	H-5→L (13 %)
	230.82	43323	5.371	0.0024	H→L+3 (46 %) H-1→L+4 (20 %)	H-2→L+4 (10 %) H-1→L+3 (5 %) H→L (6 %) H→L+4 (4 %)
	229.5	43572	5.402	0.0017	H-4→L+1 (49 %) H-2→L+2 (19 %)	H-5→L+2 (6 %) H-3→L+2 (17 %) H-1→L+2 (3 %)
Toluene	254.62	39274	4.869	0.0002	H-7→L (41 %) H-6→L (44 %)	H-5→L (13 %)

(*continued on next page*)

Table 3 (*continued*)

Solvents	λ (nm)	Wavenumber (cm^{-1})	E (eV)	f	Major contributions	Minor contributions
	230.82	43323	5.371	0.0026	H→L+3 (46 %)	H-3→L+4 (2 %) H-2→L+4 (8 %) H-1→L+3 (5 %)
					H-1→L+4 (21 %)	H→L (6 %) H→L+4 (4 %)
	229.48	43576	5.402	0.0018	H-4→L+1 (50 %) H-2→L+2 (22 %)	H-5→L+2 (5 %) H-3→L+2 (14 %) H-1→L+2 (3 %)

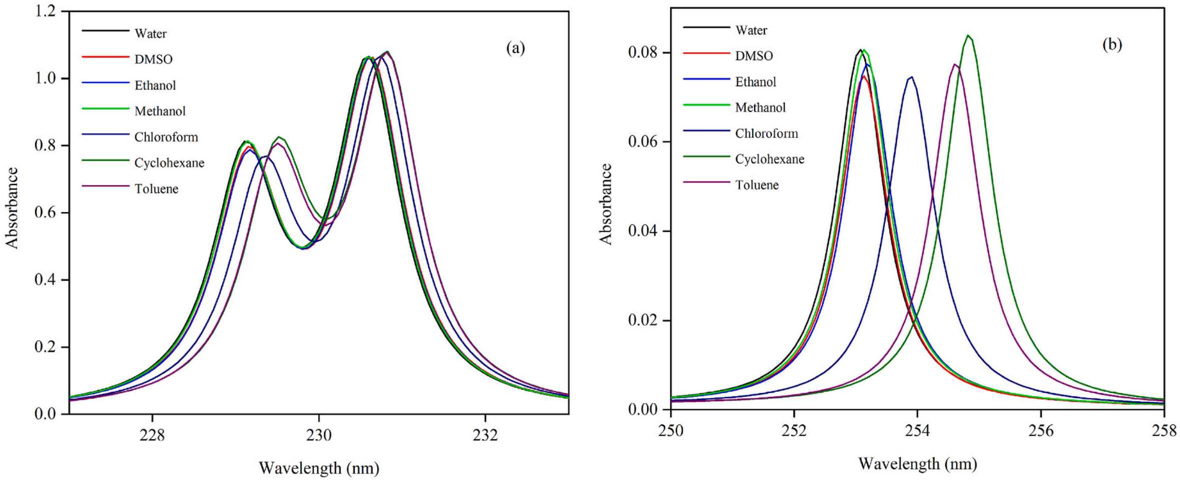

Fig. 4. Simulated electronic spectra of RCL in polar and non-polar solvents for (a) *227* – 233 nm and (b) *250*–258 nm.

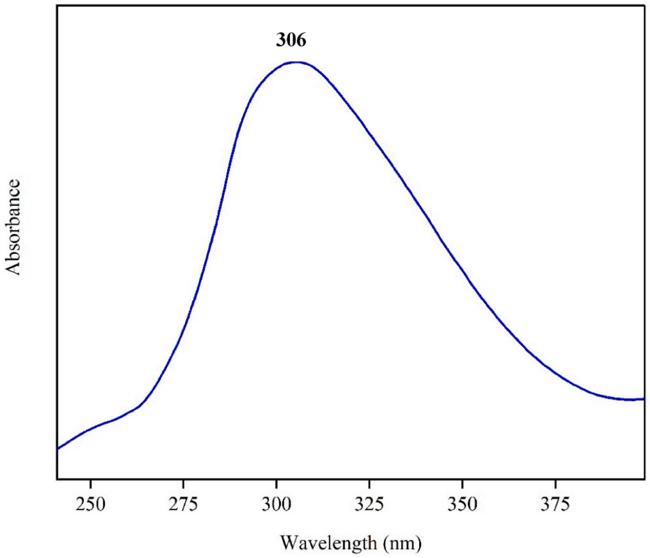

Fig. 5. Experimental electronic spectrum of RCL.

display the FMO plots for RCL in both polar and non-polar solvents, where the negative and positive regions are shown by black and green, respectively. The corresponding FMO energy gap values along with other parameters summarized in Table S1 (Supplementay material). The HOMO values range from −6.54434 eV in cyclohexane to −6.59958 eV in water, while LUMO values vary from −0.55756 eV in cyclohexane to −0.63158 eV in water. The energy gap of RCL was simulated to be 5.96827 eV in DMSO, 5.96882 eV in ethanol, 5.96854 eV in methanol, 5.96800 eV in water, 5.97535 eV in chloroform, 5.98678 eV in cyclohexane, and 5.98378 eV in toluene. Despite minor numerical differences, these variations are not prominently reflected in the orbital plots due to limited solvation effects and similar electronic environments among solvents. The larger energy gaps observed in non-polar solvents suggest that RCL demonstrates enhanced stability in these media compared to polar environments.

The electron affinity (A) and ionization potential (I), derived from the FMO energies, exhibit slight variations across solvents. The ionization potential ranges from 6.54434 eV in cyclohexane to 6.59958 eV in water, while the electron affinity varies from 0.55756 eV in cyclohexane to 0.63158 eV in water. These differences influence RCL's ability to gain or lose electrons, impacting its reactivity. Electronegativity (χ) is slightly higher in polar solvents, ranging from 3.55095 eV in cyclohexane to 3.61558 eV in water, suggesting an increased tendency to attract electrons in polar environments. Chemical hardness (η) remains relatively stable, with a slight decrease in polar solvents (2.9840 eV in water compared to 2.99339 eV in cyclohexane), while chemical softness (s) varies slightly, from 0.16703 eV^{-1} in cyclohexane (lowest) to 0.16756 eV^{-1} in water (highest), confirming greater reactivity in polar media. The global electrophilicity index (ω) and maximum electron charge transfer (ΔNmax) are larger in water and smaller in cyclohexane, reinforcing the enhanced electrophilic nature of RCL in polar solvents. These results indicate that RCL is more stable in non-polar environments and more reactive in polar environments due to increased electron transfer potential. The Density of States (DOS) spectra for RCL in different solvents, shown in Figs. S3 and S4 (Supplementary Material), remain consistent across solvents, in agreement with the FMO analysis.

3.4. Natural Bond Orbital (NBO)

NBO analysis was employed to examine charger transfer and molecular interactions in the RCL structure. The computed results in Table 4, highlights the roles of lone pair (LP) interactions, π-π* conjugation, and heteroatom-mediated charge transfer in stabilizing the molecular system. LP interactions play a important role in stabilizing the

Table 4
Second order perturbation theory of Fock matrix in selected NBO basis for RCL.

Donor (i)	Type	Acceptor (j)	Type	Transition	E(2)[a] (kJ/mol)	E(j)-E(i)[b] (a.u)	F(i,j)[c] (a.u)
C_{10}–C_{12}	π	C_{13}–C_{16}	π*	π- π*	19.64	0.28	0.067
C_{10}–C_{12}	π	C_{15}–C_{17}	π*	π- π*	21.45	0.28	0.069
C_{13}–C_{16}	π	C_{10}–C_{12}	π*	π- π*	20.76	0.28	0.069
C_{13}–C_{16}	π	C_{15}–C_{17}	π*	π- π*	20.36	0.28	0.067
C_{15}–C_{17}	π	C_{10}–C_{12}	π*	π- π*	19.38	0.29	0.067
C_{15}–C_{17}	π	C_{13}–C_{16}	π*	π- π*	20.00	0.28	0.067
C_{21}–C_{23}	π	C_{24}–C_{26}	π*	π- π*	19.52	0.29	0.067
C_{21}–C_{23}	π	C_{23}–C_{27}	π*	π- π*	19.87	0.28	0.067
C_{24}–C_{26}	π	C_{21}–C_{23}	π*	π- π*	20.66	0.28	0.068
C_{24}–C_{26}	π	C_{23}–C_{27}	π*	π- π*	20.40	0.28	0.068
C_{25}–C_{27}	π	C_{21}–C_{23}	π*	π- π*	20.35	0.28	0.068
C_{25}–C_{27}	π	C_{24}–C_{26}	π*	π- π*	19.55	0.28	0.067
S_1	L(2)	O_5–C_{19}	π*	L(2)-π*	12.85	0.23	0.079
O_2	L(2)	N_6–C_{11}	σ*	L(2)-σ*	25.18	0.71	0.122
O_2	L(2)	C_7–C_{11}	σ*	L(2)-σ*	20.20	0.61	0.101
O_3	L(2)	O_4–C_{18}	π*	L(2)-π*	48.04	0.34	0.115
O_4	L(1)	O_3–C_{18}	σ*	L(2)-π*	34.31	0.63	0.133
O_4	L(2)	C_{14}–C_{18}	σ*	L(2)-σ*	19.90	0.63	0.102
O_5	L(2)	S_1–C_{19}	σ*	L(2)-σ*	33.84	0.43	0.109
O_5	L(2)	C_{19}–C_{22}	σ*	L(2)-σ*	17.89	0.64	0.099
N_6	L(1)	O_2–C_{11}	π*	L(2)- π*	49.21	0.32	0.112

[a] E(2) – Mean energy of hyper-conjugative interactions (stabilization energy).
[b] E(j)-E(i) – Energy difference between donor (i) and acceptor (j) natural bonding orbitals.
[c] F(i,j) – Fock matrix element between i and j natural bonding orbital.

electronic structure of RCL. Among these, the N_6 (L1) → O_2–C_{11} (π*) interaction exhibits the highest stabilization energy of 49.21 kJ/mol, indicating a strong intramolecular charge transfer, where nitrogen acts as a key electron donor. Similarly, the O_3 (L2) → O_4–C_{18} (π*) interaction, with a stabilization energy of 48.04 kJ/mol, highlights efficient electron delocalization between oxygen atoms, further contributing to molecular stability. Sulfur and oxygen also participate in stabilization through LP-π* and LP-σ* interactions, as observed in S_1 (L2) → O_5–C_{19} (π*) (12.85 kJ/mol) and O_5 (L2) → S_1–C_{19} (σ*) (33.84 kJ/mol). Additionally, π-π* interactions between conjugated carbon-carbon bonds contribute to electronic stabilization, with energies ranging from 19.38 to 21.45 kJ/mol. The highest stabilization is observed in the C_{10}–C_{12} → C_{15}–C_{17} through π-π* interaction with an energy of 21.45 kJ/mol, suggesting strong electron delocalization within the conjugated system. The energy differences E(j)-E(i) range from 0.23 to 0.71 a.u, with lower values signifying more efficient charge transfer. Furthermore, the Fock matrix elements F(i,j) reveal the strongest electronic coupling in the O_4 (L1) → O_3–C_{18} (σ*) (0.133 a.u) and O_2 (L2) → N_6–C_{11} (σ*) (0.122 a.u) interactions.

3.5. Mulliken charges

Mulliken population analysis is a quantum chemistry technique that helps elucidate the distribution of electrons among atoms in molecular structures. It provides valuable insights into charge distribution and bonding properties [60]. The charge distribution of RCL is listed in Table S2 (Supplementary Material) and illustrated in Fig. 6. This analysis reveals that heteroatoms, particularly sulfur (S_1), oxygen (O_2, O_3, O_4, and O_5), and nitrogen (N_6), carry significant partial charges, indicating their strong electronegativity and involvement in intramolecular charge transfer. Among these, nitrogen (N_6) exhibits the highest negative charge (−0.53009e). It is connected to H_{33}, the carbonyl carbon (C_{11}) through C_{11}═O_2, and the methylene carbon (C_{14}) carrying H_{36} and H_{37}, suggesting its role as a key electron donor in stabilizing the molecular system. Similarly, oxygen atoms display substantial negative charges, with O_2 (−0.52258e) having the highest electron density, followed by O_3 (−0.47655e), O_4 (−0.47008e), and O_5 (−0.42466e). Carbon atoms exhibit a diverse range of partial charges, with carbonyl carbons C_{19} (0.24568e), C_{11} (0.61265e), and C_{18} (0.61966e) carrying the highest positive charges. Atoms with high negative charges, such as oxygen (O_2, O_3, O_4, O_5) and nitrogen (N_6), have high electron density, making them strong nucleophilic centers. These atoms can participate in nucleophilic interactions by donating their lone pairs of electrons to electrophilic centers, such as carbonyl carbons (C_{11}, C_{18}, and C_{19}), which have high positive charges and are more likely to accept electrons. Additionally, several methyl and methylene carbon atoms, such as C_8 (−0.25099e), C_9 (−0.36664e), and C_{22} (−0.3737e), exhibit considerable negative charges. In contrast, sulfur (S_1), bonded to a carbonyl group and a methylene group, carries a low positive charge (0.14006e), indicating moderate electron-withdrawing behavior. The carbonyl oxygen withdraws electron density from sulfur, increasing its electron deficiency, while the methylene group donates some electron density back, partially couteracting this effect and preventing excessive positive charge buildup. All hydrogen atoms exhibit positive charges, with H_{33} (0.27385e) carrying the highest due to strong polarization from its attachment to nitrogen (N_6).

3.6. Influence of solvents on Molecular Electrostatic Potential (MEP)

In computational chemistry, the MEP correlated with electron density is key for identifying nucleophilic and electrophilic reactive sites and visualizing molecular charge distribution [61]. The calculated MEP values for RCL in different solvents (polar and non-polar) are as follows; -6.751×10^{-2} to 6.751×10^{-2} e.s.u. (DMSO), -6.703×10^{-2} to 6.703×10^{-2} e.s.u. (ethanol), -6.727×10^{-2} to 6.727×10^{-2} e.s.u. (methanol), -6.773×10^{-2} to 6.773×10^{-2} e.s.u. (water), and -6.363×10^{-2} to 6.363×10^{-2} e.s.u. (chloroform), -6.006×10^{-2} to 6.006×10^{-2} e.s.u. (cyclohexane), and -6.085×10^{-2} to 6.085×10^{-2} e.s.u. (toluene). The MEP map highlights key reactive sites: the oxygen atoms in the

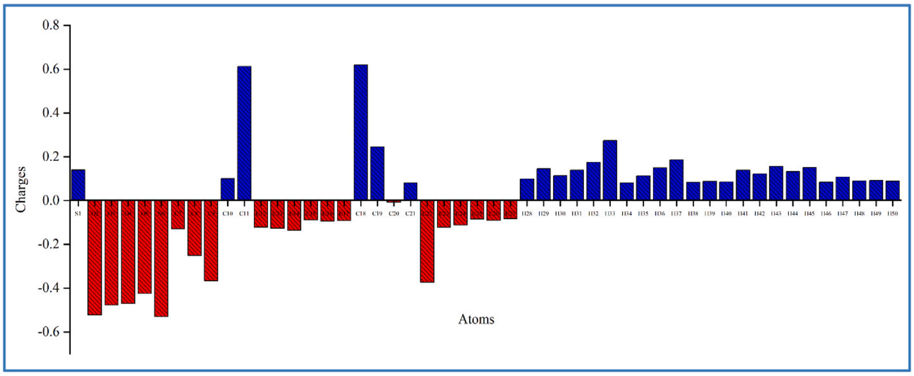

Fig. 6. Mulliken charge distributions of RCL.

cabonyl (C═O) groups appear as red regions, indicating high electron density and susceptibility to electrophilic attack. The cyclic structure is represented in green, signifying neutral potential. Meanwhile, blue regions appear over hydrogen atoms at the molecular boundaries, marking sites for nucleophilic interactions. The MEP color maps of RCL in different solvents are depicted in Figs. S5 and S6 (Supplementary Material). Despite varying MEP values, the color map remains consistent across solvents, most likely as a result of minor solvation effects and electrostatic shifts. The Mulliken charge distribution confirms the reactive sites identified by MEP.

3.7. Topological analysis

3.7.1. ELF and LOL

The ELF and LOL are essential simulation methods used to understand the chemical bonding, orbitals distribution, and delocalized and localized regions within the molecular structures. The color-filled, contour, and shaded map with a projection of ELF and LOL for RCL were shown in Figs. 7 and 8. In the color-filled map, red (localized) and blue (delocalized) signify higher and lower LOL values. Electrons exhibit significant delocalization in the highest value range of 0–1, suggesting the presence of lone pairs or covalent bonds. On the other hand, electrons that should be delocalized show lower values below 0.5. In the present findings, the red hue over the hydrogens H_{30}, H_{42}, and H_{44} signifies the prominent electron-localized regions. Similarly, the blue hues around the nitrogen (N_6) and carbon atoms C_7, C_{22}, and C_{24} highlight the electron depletion region. The LOL and ELF maps confirm the intra and intermolecular delocalization of charges within the molecular structure of RCL.

3.7.2. RDG and NCI

RDG and NCI are powerful tools for analyzing non-covalent interactions (steric repulsions, hydrogen bonding, and van der Walls forces) within chemical structures [62,63]. The color and iso-surface

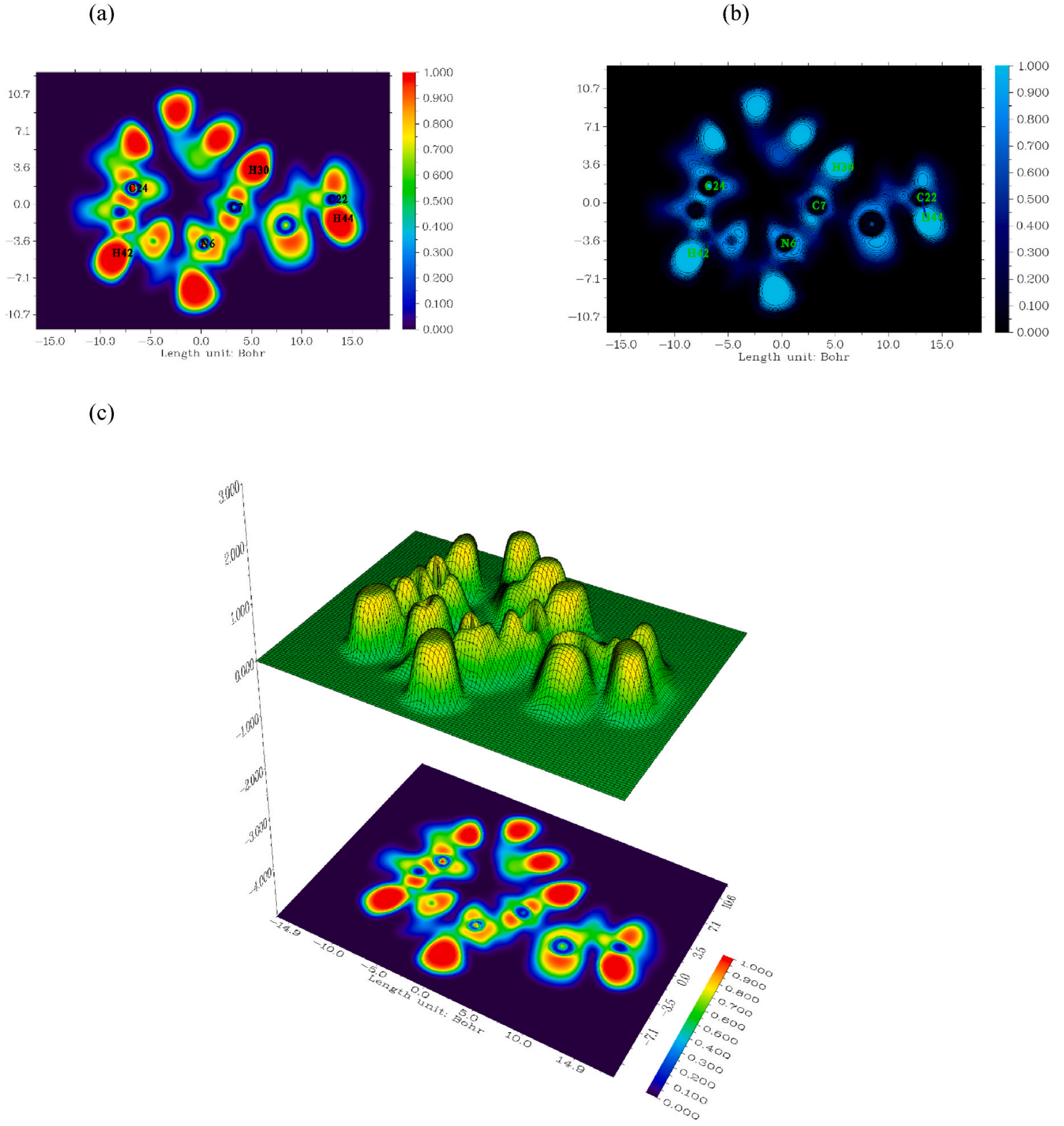

Fig. 7. (a) ELF diagram with numbering, (b) contour map, and (c) ELF diagram with projection scheme of RCL.

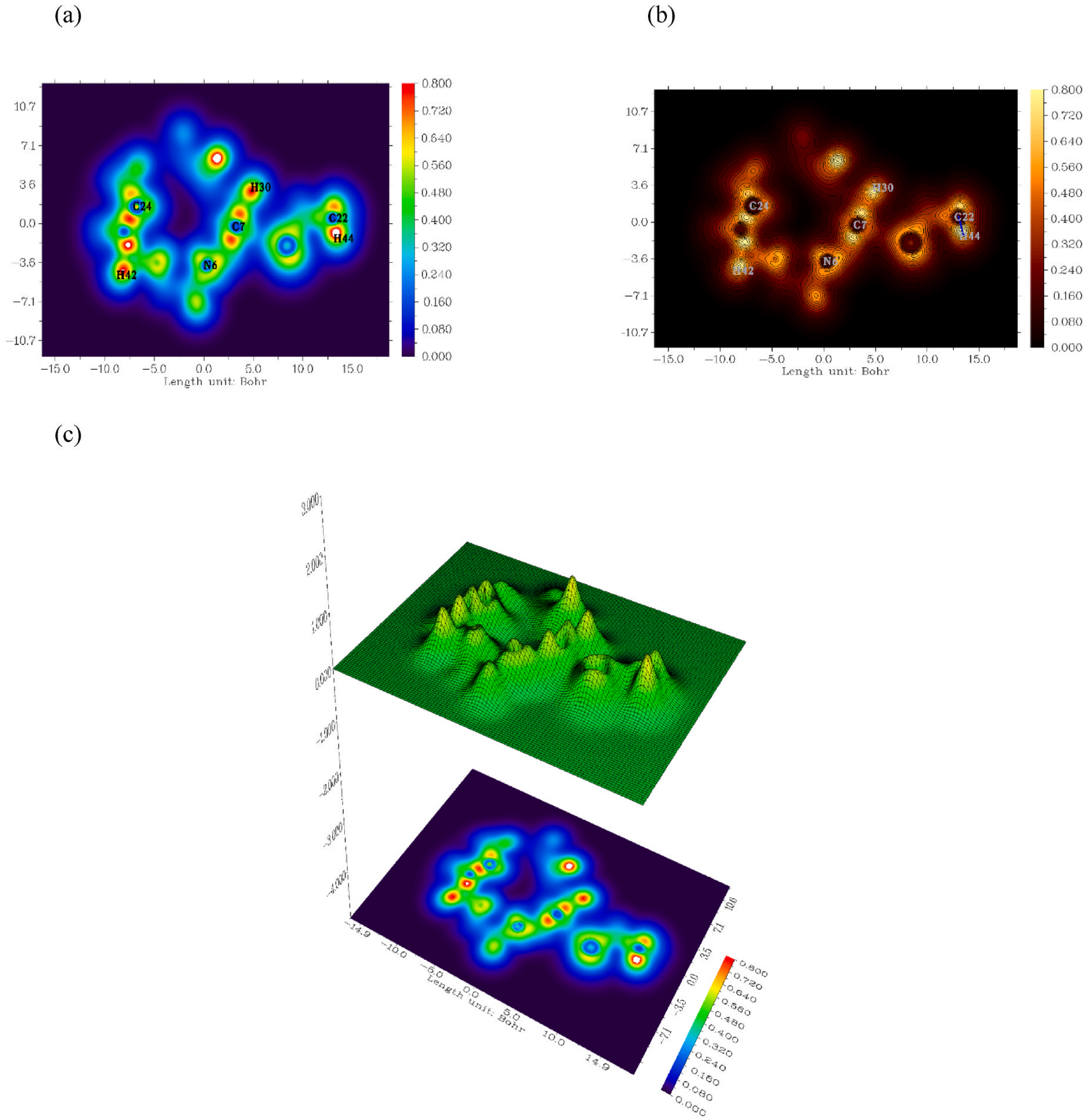

Fig. 8. (a) LOL diagram with numbering, (b) contour map, and (c) ELF diagram with projection scheme of RCL.

maps of RDG and NCI of RCL have been presented in Fig. 9. In NCI, the color map represents the repulsive and attractive interactions of RCL, while the RDG color map indicates its solidity and reactivity. The findings highlight the hydrogen bonding, van der Walls interaction, and steric effect between −0.05 and −0.023 a.u (blue), −0.01 to −0.018 (green), and 0.013 to 0.05 a.u. (red), respectively. In the NCI iso-surface map, the red colors at the center of the aromatic rings and neighboring oxygen and nitrogen atoms confirms the solid repulsion. In the same way, the green colors between the ring structures and near the acetylthio group signify the van der Walls interaction in the molecular structure of RCL.

3.8. Drug-likeness

The ADME (Absorption, Distribution, Metabolism, and Excretion) characteristics of RCL were evaluated using the online SwissADME tool to simulate its pharmacokinetic parameters. Lipinski's rule of five outlines key criteria for drug-like properties, stating that a compound should have no more than 10 hydrogen bond acceptors and 5 hydrogen bond donors, a molecular weight below 500 Da, and TPSA and logP values under 140 Å^2 and 5, respectively [64]. The simulated ADME radar and boiled egg view of RCL are presented in Figs. S7 and S8 (Supplementay material), and the corresponding numerical findings are tabulated in Table S3 (Supplementay material). The estimated molecular weight of RCL is 385.48 g/mol, with four hydrogen bond acceptors and a single hydrogen bond donor. The logP value was simulated at 2.60 mg/ml, and the TPSA value was 97.77 Å^2, indicating high gastrointestinal absorption (GI) and limited blood-brain barrier (BBB) permeability. These findings confirm RCL's drug-likeness and provide insights into its potential pharmacokinetic behavior.

3.9. Molecular docking

Molecular docking is a computational approach widely applied in drug design, and structural biology to evaluate the binding energy between a receptor (such as a protein or DNA) and a ligand at the atomic level, facilitating the formation of a stable complex [65,66]. The X-ray diffraction (XRD) crystal structures of SARS-CoV-2 main proteases and

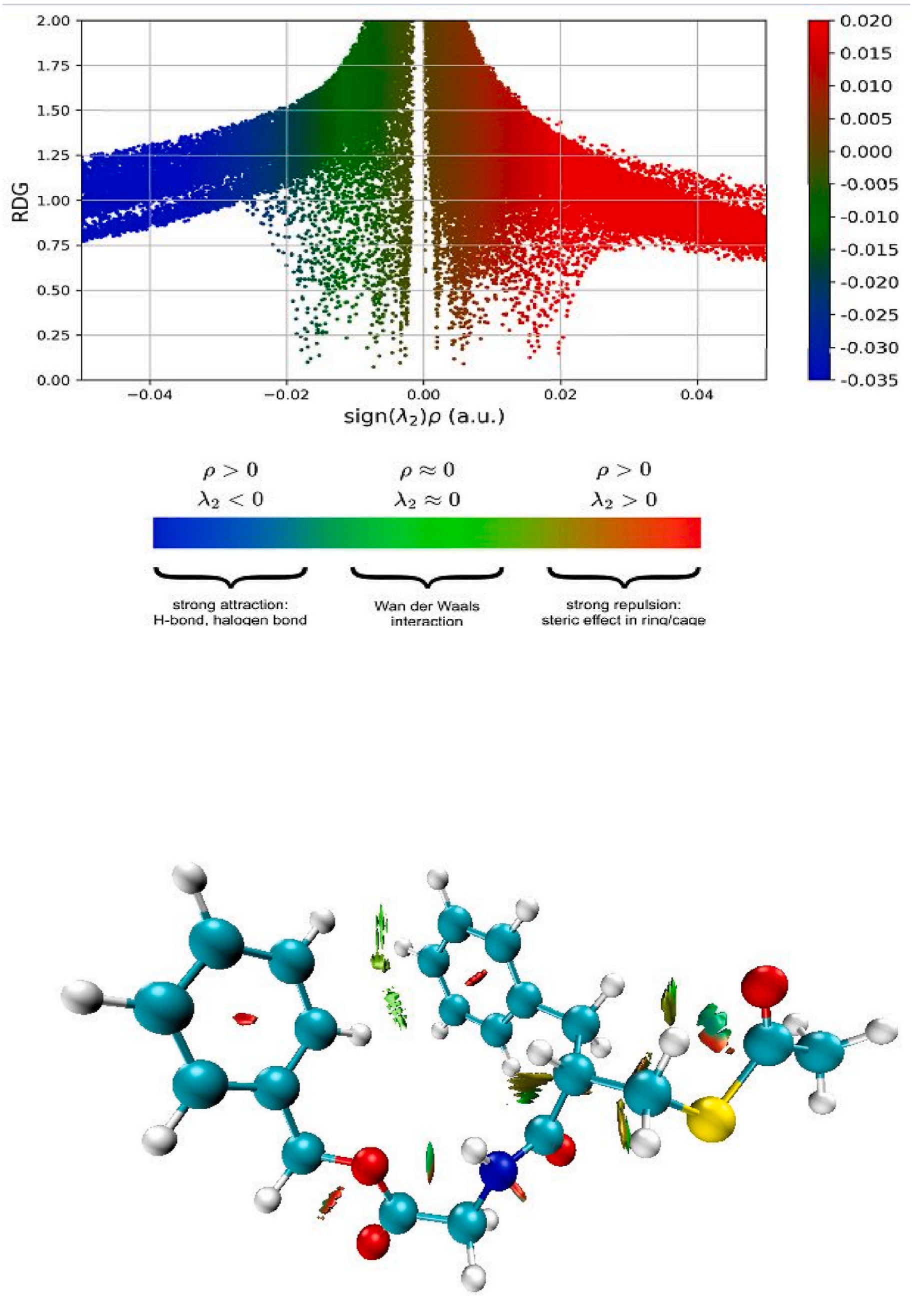

Fig. 9. RDG scatter graph (*top*) and NCI diagram (*bottom*) of RCL.

spike glycoprotein (PDB IDs: 6LU7 and 6VXX) with resolutions of 2.16 Å and 2.80 Å, along with SMAD proteins (PDB IDs: 1U7F and 1U7V) with resolutions of 2.60 Å and 2.70 Å, were obtained from the Protein Data Bank (PDB). The water molecules and unnecessary coordinates were removed from the crystal structure of the main proteases, and the files were converted to PDBQT format. The ligand structure RCL was optimized employing the GaussView 6 program and kept in PDBQT format. In the present assessment, the RCL (ligand) was docked with 6LU7, 6VXX, IU7F, and 1U7V proteins (macromolecule), with the results summarized in Table 5 and visualized in Fig. 10. From the findings, RCL shows a binding affinity (kcal mol^{-1})of −8.08 (6LU7), −3.34 (6VXX), −6.51 (1U7F), and −6.62 (1U7V) by forming hydrophobic interactions and hydrogen bondings with active side amino acids. The target proteins (6LU7 and 6VXX) are responsible for viral replication by forming a stable complex, a key target for COVID-19 treatment. Additionally, SMAD proteins (1U7F and 1U7V) serve as intracellular transcriptional regulators and signal transducers in the TGF-β signaling pathway, which regulates essential cellular processes such as apoptosis, differentiation, migration, and proliferation. These functions align with RCL's antiviral and antiproliferative properties, underscoring its role in regulating viral responses and cell growth.

3.10. *Thermodynamical properties*

The thermodynamical parameters of RCL are interconnected and provide a comprehensive understanding of its stability and behavior. From Table S4 (Supplementay material), the Self-Consistent Field (SCF) energy of −1567.986 Hartree reflects a stable electronic structure, contributing to the molecule's overall stability. This stability influences other thermodynamic properties, including the total thermal energy (270.855 kcal mol^{-1}) and vibrational energy (269.078 kcal mol^{-1}), which describe the molecule's vibrational motions. The zero-point

Table 5
Ligand – protein interactions of RCL.

Ligand	Protein	Binding score (kcal mol^{-1})	Hydrogen bonding	Bond distance (Å)	Hydrophobic interactions
Racecadotril	6LU7	−8.08	Lysine 137	2.2	Tyrosine 126 Serine 139 Glycine 138
			Lysine 5	2.82, 3.02	Glutamine 127 Glutamic acid 290
	1U7F	−6.51	Asparagine 265	3.24	Asparagine 401 Leucine 273 Phenylaniline 269, 231, 248 Serine 234 Proline 263 Histidine 249 Glutamine 246 Threonine 247 Arginine 268 Aspartic acid 262 Cysteine 270
	1U7V	−6.62	Glutamine 334	2.91	Valine 333, 335 Histidine 371
			Arginine 285	3.02	Asparagine 369, 318 Glutamine 284
			Arginine 285	3.15	Valine 319, 286 Serine 317
	6VXX	−3.34	Threonine 768	3.30	Asparagine 764 Threonine 761
			Glutamine 314	2.83	Glycine 769 Leucine 303
			Arginine 765	2.98	Tyrosine 313

vibrational energy (ZPVE) of 253.970 kcal mol^{-1}, representing the energy at the lowest vibrational state, further indicates inherent stability. The specific heat capacity (Cv) of 98.003 cal mol^{-1}K^{-1} reveals how much heat the molecule can absorb before its temperature changes significantly, related to its vibrational and rotational motions. The entropy value of 195.611 cal mol^{-1}K^{-1} measures the degree of disorder or randomness, influenced by the molecule's vibrational, rotational, and translational motions. The dipole moment of 3.3014 Debye, with components $\mu_x = -1.2008$ Debye, $\mu_y = 1.2422$ Debye, and $\mu_z = 2.8132$ Debye, highlights the asymmetric charge distribution and its effects on molecular interactions and solubility. Finally, the rotational constants (X = 0.2463 GHz, Y = 0.0964 GHz, Z = 0.0839 GHz) describe the rotational frequencies about the molecule's principal axes, influencing its rotational dynamics and interactions with external fields.

4. Conclusion

The sulfur-containing compound racecadotril (RCL) has been extensively studied through theoretical and experimental approaches. In the optimized geometry, 51 bond distances and 86 bond angles were identified, with the maximum bond distance from C–H (22 bonds) and the maximum bond angle from C–C–H (37 angles). Vibrational wavenumbers affirm the occurrence of NH, CH, CH_2, CH_3, CO, CC, and CS groups. Non-polar solvents exhibit a higher FMO energy gap (5.9753–5.9867 eV), indicating greater stability, whereas polar solvents have a lower energy gap (5.9680–5.9688 eV), resulting in increased chemical reactivity. In the NBO analysis, the N_6 (L_1) → O_2–C_{11} (π^*) interaction shows the highest stabilization energy (49.21 kJ/mol), indicating strong intramolecular charge transfer with nitrogen as the key electron donor. Similarly, the O_3 (L_2) → O_4–C_{18} (π^*) interaction (48.04 kJ/mol) enhances electron delocalization between oxygens, boosting molecular stability. Mulliken charge distribution analysis reveals that nitrogen (N_6) and oxygen (O_2, O_3, O_4, O_5) act as nucleophilic centers due to their high negative charges, while carbonyl carbons (C_{11}, C_{18}, C_{19}) serve as electrophilic centers with high positive charges. Sulfur (S_1) shows moderate electron-withdrawing behavior, and H_{33} carries the highest positive charge due to nitrogen polarization, consistent with MEP analysis. Localized, delocalized, and weak interactions were detected within the molecule using topological analysis. The thermodynamic analysis confirms molecular stability with an SCF energy of −1567.986 Hartree and a dipole moment of 3.3014 Debye. The drug-likeness of RCL is supported by ADME analysis, while molecular docking revealed binding energies (kcal mol^{-1}) of −8.08 (6LU7), −3.34 (6VXX), −6.51 (1U7F), and −6.62 (1U7V), indicating its potential antiviral and antiproliferative activity. These findings provide a

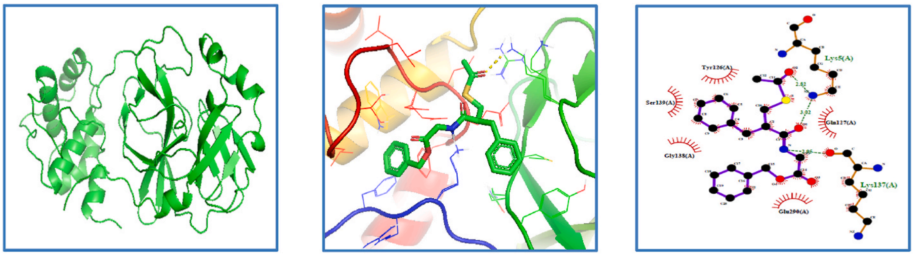

Fig. 10 (a). The 3D PyMOL and 2D LigPlot $^+$ view of RCL against 6LU7 protein.

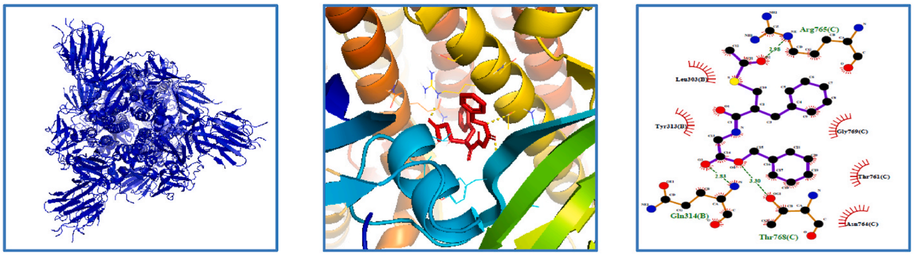

Fig. 10 (b). The 3D PyMOL and 2D LigPlot $^+$ view of RCL against 6VXX protein.

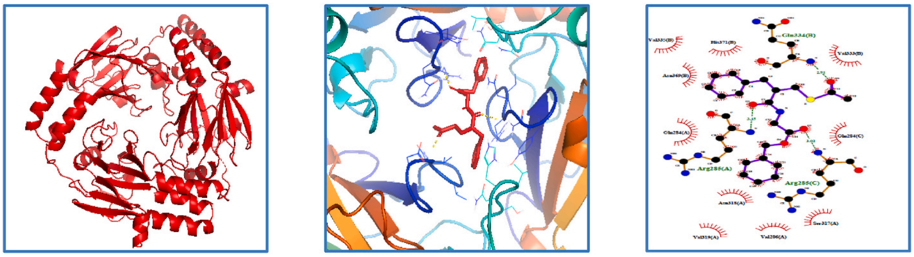

Fig. 10 (c). The 3D PyMOL and 2D LigPlot $^{+}$ view of RCL against 1U7V protein.

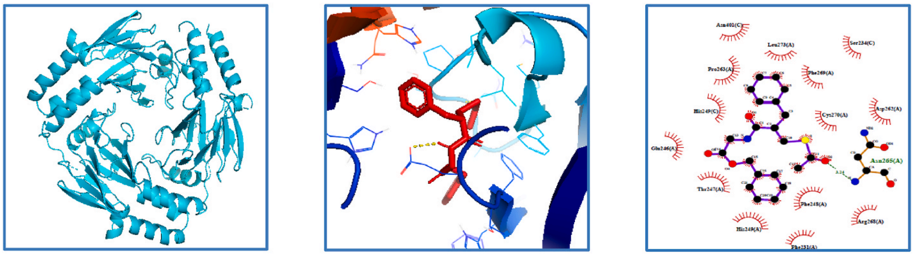

Fig. 10 (d). The 3D PyMOL and 2D LigPlot $^{+}$ view of RCL against 1U7F protein.

foundation for developing new treatments for viral infections and antiproliferative therapies.

CRediT authorship contribution statement

R. Manjula: Writing – original draft, Data curation, Conceptualization. **C. Pavithra:** Writing – review & editing, Supervision, Resources. **A. Ram Kumar:** Writing – review & editing, Methodology, Investigation. **K. Durgadevi:** Visualization, Validation, Data curation. **Babu Balraj:** Visualization, Validation, Conceptualization. **S. Selvaraj:** Writing – review & editing, Methodology, Formal analysis.

Conflict of interest

The authors declare that there are no conflicts of interest regarding the publication of this manuscript.

Acknowledgment

The authors thank Alagappa University, Karaikudi, for performing FT-Raman and UV–Vis spectroscopy, and IIT Madras, Chennai, for performing FT-IR spectroscopy.

Appendix A. Supplementary data

Supplementary data to this article can be found online at https://doi.org/10.1016/j.jics.2025.101702.

References

[1] S. Pathania, R.K. Narang, R.K. Rawal, Role of sulphur-heterocycles in medicinal chemistry: an update, Eur. J. Med. Chem. 180 (2019) 486–508, https://doi.org/10.1016/j.ejmech.2019.07.043.

[2] M. Feng, B. Tang, S. H Liang, X. Jiang, Sulfur containing scaffolds in drugs: synthesis and application in medicinal chemistry, Curr. Top. Med. Chem. 16 (11) (2016) 1200–1216, https://doi.org/10.2174/1568026615666150915111741.

[3] M.A. Marcinkowska, H.H. Jeleń, Role of sulfur compounds in vegetable and mushroom aroma, Molecules 27 (18) (2022) 6116, https://doi.org/10.3390/molecules27186116.

[4] L. Schutte, R. Teranishi, Precursors of sulfur-containing flavor compounds, Crit. Rev. Food Sci. Nutr. 4 (4) (1974) 457–505, https://doi.org/10.1080/10408397409527166.

[5] A. Sharma, L.R. Singh, An insight into the pharmacology of sulphur containing peptide drugs, Eur. J. Med. Chem. 271 (2024) 116456, https://doi.org/10.1016/j.ejmech.2024.116456.

[6] D. Imhof, D. Roy, F. Albericio, Chemical design and biomedical applications of disulfide-rich peptides: challenges and opportunities, Front. Chem. 8 (2020) 586377, https://doi.org/10.3389/fchem.2020.586377.

[7] D.E. Kim, Y. Kim, D.H. Cho, S.Y. Jeong, S.B. Kim, N. Suh, J.S. Lee, E.K. Choi, J. Y. Koh, J.J. Hwang, C.S. Kim, Raloxifene induces autophagy-dependent cell death in breast cancer cells via the activation of AMP-activated protein kinase, Mol. Cells 38 (2) (2015) 138–144, https://doi.org/10.14348/molcells.2015.2193.

[8] R.K. Rawal, V. Murugesan, S.B. Katti, Structure-activity relationship studies on clinically relevant HIV-1 NNRTIs, Curr. Med. Chem. 19 (31) (2012) 5364–5380, https://doi.org/10.2174/092986712803833326.

[9] M.T. Herdeiro, S. Soares, T. Silva, F. Roque, A. Figueiras, Impact of rosiglitazone safety alerts on oral antidiabetic sales trends: a countrywide study in Portugal, Fund. Clin. Pharmacol. 30 (5) (2016) 440–449, https://doi.org/10.1111/fcp.12207.

[10] M. Seide, M. Marion, M.A. Mateescu, D.A. Averill-Bates, The fungicide thiabendazole causes apoptosis in rat hepatocytes, Toxicol. Vitro 32 (2016) 232–239, https://doi.org/10.1016/j.tiv.2015.12.018.

[11] M. Eberlin, T. Mück, M.C. Michel, A comprehensive review of the pharmacodynamics, pharmacokinetics, and clinical effects of the neutral endopeptidase inhibitor racecadotril, Front. Pharmacol. 3 (2012) 93, https://doi.org/10.3389/fphar.2012.00093.

[12] D.M. Lambert, F. Mergen, J.H. Poupaert, P. Dumont, Analgesic potency of S-acetylthiorphan after intravenous administration to mice, Eur. J. Pharmacol. 243 (2) (1993) 129–134, https://doi.org/10.1016/0014-2999(93)90371-N.

[13] Y. Xu, J. Huang, F. Liu, S. Gao, Q. Guo, Quantitative analysis of racecadotril metabolite in human plasma using a liquid chromatography/tandem mass spectrometry, J. Chromatogr. B 852 (1–2) (2007) 101–107, https://doi.org/10.1016/j.jchromb.2006.12.041.

[14] F. Xu, L. Yang, G. Xu, A rapid and validated HPLC method to quantify racecadotril metabolite, thiorphan, in human plasma using solid-phase extraction, J. Chromatogr. B 861 (1) (2008) 130–135, https://doi.org/10.1016/j.jchromb.2007.11.038.

[15] A. Wilder-Smith, C.J. Chiew, V.J. Lee, Can we contain the COVID-19 outbreak with the same measures as for SARS? Lancet Infect. Dis. 20 (5) (2020) e102–e107, https://doi.org/10.1016/S1473-3099(20)30129-8.

[16] T. Kronenberger, S.A. Laufer, T. Pillaiyar, COVID-19 therapeutics: small-molecule drug development targeting SARS-CoV-2 main protease, Drug Discov. Today 28 (6) (2023) 103579, https://doi.org/10.1016/j.drudis.2023.103579.

[17] D. Wu, T. Wu, Q. Liu, Z. Yang, The SARS-CoV-2 outbreak: what we know, Int. J. Infect. Dis. 94 (2020) 44–48, https://doi.org/10.1016/j.ijid.2020.03.004.

[18] A.G. Harrison, T. Lin, P. Wang, Mechanisms of SARS-CoV-2 transmission and pathogenesis, Trends Immunol. 41 (12) (2020) 1100–1115, https://doi.org/10.1016/j.it.2020.10.004.

[19] X. Pang, W. Xu, Y. Liu, H. Li, L. Chen, The research progress of SARS-CoV-2 main protease inhibitors from 2020 to 2022, Eur. J. Med. Chem. 257 (2023) 115491, https://doi.org/10.1016/j.ejmech.2023.115491.

[20] W.C. Chiou, M.S. Hsu, Y.T. Chen, J.M. Yang, Y.G. Tsay, H.C. Huang, C. Huang, Repurposing existing drugs: identification of SARS-CoV-2 3C-like protease inhibitors, J. Enzym. Inhib. Med. Chem. 36 (1) (2021) 147–153, https://doi.org/10.1080/14756366.2020.1850710.

[21] A. Ram Kumar, S. Selvaraj, A.S. Vickram, G.S. Mol, S. Awasthi, M. Thirunavukkarasu, M. Selvaraj, S. Basumatary, Exploring the potential of diosgenin as a promising antitumor agent through comprehensive spectroscopic characterization, solvent-solute interactions, topological properties, Hirshfeld surface, and molecular docking interactions with 2NZT and 2I1V proteins, Spectrochim. Acta Mol. Biomol. Spectrosc. 327 (2024) 125349, https://doi.org/10.1016/j.saa.2024.125349.

[22] P. Divya, V.S. Jeba Reeda, S. Renuga, C. Devi Annapoorani, V. Bena Jothy, Vibrational analysis, DFT computations of spectroscopic, non-covalent analysis with molecular docking and dynamic simulation of 2-amino-4, 6-dimethyl pyrimidine benzoic acid, J. Mol. Struct. 1318 (2024) 139160, https://doi.org/10.1016/j.molstruc.2024.139160.

[23] V.S. Jeba Reeda, P. Divya, A. Amala Jeya Ranchani, A. Manikandan, Shakeel Alvi, Rashid Ali, Nazia Siddiqui, Nazrul Haq, S. Muthu, Ray Butcher, Saleem Javed, Comprehensive analysis of 2, 5-dimethyl-1-(naphthalen-1-yl)-1H-pyrrole: X-ray crystal structure, spectral, computational, molecular properties, docking studies, molecular dynamics, and MMPBSA, J. Mol. Struct. 1321 (2025) 140062, https://doi.org/10.1016/j.molstruc.2024.140062.

[24] K. Thirunavukkarasu, P. Rajkumar, S. Selvaraj, S. Gunasekaran, S. Kumaresan, Electronic structure, vibrational (FT-IR and FT-Raman), UV–Vis and NMR analysis of 5-(4-(2-(5-ethylpyridin-2-yl) ethoxy) benzyl) thiazolidine-2, 4-dione by quantum chemical method, Chemical Data Collections 17 (2018) 263–275, https://doi.org/10.1016/j.cdc.2018.09.006.

[25] A. Srivastava, R. Mishra, P. Tandon, A.K. Bansal, FT-Raman, FT-IR, UV spectroscopic, NBO and DFT quantum chemical study on the molecular structure, vibrational and electronic transitions of clopidogrel hydrogen sulfate form 1: a comparison to form 2, Spectrochim. Acta Mol. Biomol. Spectrosc. 104 (2013) 409–418, https://doi.org/10.1016/j.saa.2012.11.093.

[26] R.S. Borges, G.R. Nagurniak, L.M. Queiroz, C.S. Maia, C.A. Barros, E. Orestes, A. B. da Silva, Structure and toxicity of clozapine and olanzapine on agranulocytosis, Med. Chem. Res. 25 (2016) 322–328, https://doi.org/10.1007/s00044-015-1484-8.

[27] S. Muthu, J.U. Maheswari, T. Sundius, Quantum mechanical, spectroscopic studies (FT-IR, FT-Raman, NMR, UV) and normal coordinates analysis on 3-([2-(diaminomethyleneamino) thiazol-4-yl] methylthio)-N′-sulfamoyl propanimidamide, Spectrochim. Acta Mol. Biomol. Spectrosc. 108 (2013) 307–318, https://doi.org/10.1016/j.saa.2013.02.022.

[28] J. Pandey, P. Prajapati, A. Srivastava, P. Tandon, K. Sinha, A.P. Ayala, A.K. Bansal, Spectroscopic and molecular structure (monomeric and dimeric model) investigation of Febuxostat: a combined experimental and theoretical study, Spectrochim. Acta Mol. Biomol. Spectrosc. 203 (2018) 1–12, https://doi.org/10.1016/j.saa.2018.05.074.

[29] M.J. Frisch, et al., Gaussian 16, Gaussian Inc, Wallingford CT, 2016.

[30] A.D. Becke, Density functional thermo chemistry – I: the effect of the exchange only gradient correlation, J. Chem. Phys. 98 (1993) 5648–5652, https://doi.org/10.1063/1.462066.

[31] C. Lee, W. Yang, R.G. Parr, Development of the Colle-Salvetti correlation-energy formula into a functional of the electron density, Phys. Rev. B 37 (1988) 785–789, https://doi.org/10.1103/PhysRevB.37.785.

[32] B. Miehlich, A. Savin, H. Stoll, H. Preuss, Results obtained with the correlation energy density functional of Becke and Lee, Yang and Parr, Chem. Phys. Lett. 157 (3) (1989) 200–206, https://doi.org/10.1016/0009-2614(89)87234-3.

[33] W. Kohn, L.J. Sham, Self-consistent equations including exchange and correlation effects, Phy, Rev. 140 (1965) A1133–A1138, https://doi.org/10.1103/PhysRev.140.A1133.

[34] R.G. Parr, W. Yang, Density-functional Theory of Atoms and Molecules, Oxford Univ. Press, Oxford, 1989, https://doi.org/10.1007/978-94-009-9027-2_2.

[35] P. Hohenberg, W. Kohn, Inhomogeneous electron gas, Phys. Rev. 136 (1964) B864–B871, https://doi.org/10.1103/PhysRev.136.B864.

[36] M. Petersilka, U.J. Gossman, E.K.U. Gross, Excitation energies from time dependent density-functional theory, Phys. Rev. Lett. 76 (1996) 1212–1215, https://doi.org/10.1103/PhysRevLett.76.1212.

[37] E. Runge, E.K.U. Gross, Density functional theory for time-dependent systems, Phys. Rev. Lett. 52 (1984) 997, https://doi.org/10.1103/PhysRevLett.52.997.

[38] R. Bauernschmitt, R. Ahlrichs, Treatment of electronic excitations within the adiabatic approximation of time dependent density functional theory, Chem. Phys. Lett. 256 (1996) 454–464, https://doi.org/10.1016/0009-2614(96)00440-X.

[39] N.M. O`Boyle, A.L. Tenderholt, K.M. Langner, cclib: a library for package-independent computational chemistry algorithms, J. Comput. Chem. 29 (2008) 839–845, https://doi.org/10.1002/jcc.20823.

[40] R. Dennington, T.A. Keith, J.M. Millam GaussView 6.0, Semichem Inc., Shawnee Mission, KS, USA, 2016.

[41] G.A. Zhurko, D.A. Zhurko, Chemcraft Program Version 1.6 (Build 315) (2009). http://www.chemcraftprog.com./.

[42] E.D. Glendening, A.E. Reed, J.E. Carpenter, F. Weinhold, NBO Version 3.1, TCI, University of Wisconsin, Madison, 1998.

[43] W.L. DeLano, Pymol: an open-source molecular graphics tool, CCP4 Newsletter on protein Crystallography 40 (1) (2002) 82–92. http://www.pymol.org.

[44] G.M. Morris, R. Huey, W. Lindstrom, M.F. Sanner, R.K. Belew, D.S. Goodsell, A. J. Olson, AutoDock4 and AutoDockTools4: automated docking with selective receptor flexibility, J. Comput. Chem. 30 (2009) 2785–2791, https://doi.org/10.1002/jcc.21256.

[45] T. Lu, F. Chen, Multiwfn: a multifunctional wavefunction analyzer, J. Comput. Chem. 33 (2012) 580–592, https://doi.org/10.1002/jcc.22885.

[46] S. Armakovic, S.J. Armakovic, Atomistica. online–web application for generating input files for ORCA molecular modelling package made with the Anvil platform, Mol. Simul. 49 (1) (2023) 117–123, https://doi.org/10.1080/08927022.2022.2126865.

[47] S. Armakovic, S.J. Armakovic, Online and desktop graphical user interfaces for xtb programme from atomistica. online platform, Mol. Simul. 50 (7–9) (2024) 560–570, https://doi.org/10.1080/08927022.2024.2329736.

[48] W. Humphrey, A. Dalke, K. Schulten, VMD:visual molecular dynamics, J. Mol. Graph. 14 (1996) 33–38, https://doi.org/10.1016/0263-7855(96)00018-5.

[49] R. Manjula, C. Pavithra, A. Ram Kumar, K. Durgadevi, B. Balraj, S. Selvaraj, Exploring structural and spectroscopic aspects, solvent effect (polar and non-polar) on electronic properties, topological insights, ADME and molecular docking study of thiocolchicoside: a promising candidate for antiviral and antitumor pharmacotherapy, Spectrochim. Acta Mol. Biomol. Spectrosc. 331 (2025) 125807, https://doi.org/10.1016/j.saa.2025.125807.

[50] I. Ragavan, C. Vidya, S. Shanavas, R. Acevedo, P.M. Anbarasan, A. Manjri, A. Prakasam, C. Sudhakar, T. Selvankumar, Synthesis, spectroscopic characterization and molecular docking study of ethyl 2-(4-(5, 9-dihydro-6-hydroxy-2-mercapto-4H-purin-8-ylthio) thiophen-2-yl)-2-oxoacetate molecule for the chemotherapeutic treatment of breast cancer cells, Chem. Phys. 530 (2020) 110596, https://doi.org/10.1016/j.chemphys.2019.110596.

[51] V. Vijayalakshmi, N. Kanagathara, Janczak Jan, M.K. Marchewka, Mohammad Azam, K. Senthilkumar, Structural, spectroscopic and second harmonic generation evaluation of 1, 2, 4-triazolinium tartrate-tartaric acid as a promising nonlinear optical material, Opt. Mater. 147 (2024) 11469, https://doi.org/10.1016/j.optmat.2023.114694.

[52] K. Guna, P. Sakthivel, I. Ragavan, A. Arunkumar, P.M. Anbarasan, M. Shkir, An experimental and computational analysis on 2, 6-diamine-7H-purine ligand with spectroscopic, AIM, NLO and biological activity, Opt Laser. Technol. 168 (2024) 109872, https://doi.org/10.1016/j.optlastec.2023.109872.

[53] R. Suja, A. Rathika, V.S. Jeba Reeda, A. Arun Kumar, P. Divya, Synthesis, spectroscopic analysis (FT-IR, FT-Raman, UV, NMR), non-covalent interactions (RDG, IGM) and dynamic simulation on Bis (8-hydroxy quinoline) salicylate salicylic acid, J. Mol. Struct. 1310 (2024) 138231, https://doi.org/10.1016/j.molstruc.2024.138231.

[54] S. Anithamani, M.K. Subramanian, I. Ragavan, P.M. Anbarasan, N.A. Siddiqui, A. Khan, Synthesis, structural mechanisms, RDG, biological and pharmaceutical significance of anticancer agent 9H-carbazole attached 4-chlorobenzaldehyde using DFT reckonings, J. Indian Chem. Soc. 101 (11) (2025) 101343, https://doi.org/10.1016/j.jics.2024.101343.

[55] N. Dege, H. Gokce, O.E. Dogan, G. Alpaslan, T. Agar, S. Muthu, Y. Sert, Quantum computational, spectroscopic investigations on N-(2-((2-chloro-4, 5-dicyano-phenyl) amino) ethyl)-4-methylbenzenesulfonamide by DFT/TD-DFT with different solvents, molecular docking and drug-likeness researches, Colloids Surf. A Physicochem. Eng. Asp. 638 (2022) 128311, https://doi.org/10.1016/j.colsurfa.2022.128311.

[56] K. Sarojini, H. Krishnan, C.C. Kanakam, S. Muthu, Synthesis, X-ray structural, characterization, NBO and HOMO–LUMO analysis using DFT study of 4-methyl-N-(naphthalene-1-yl) benzene sulfonamide, Spectrochim. Acta Part A Mol. Biomol. Spectrosc. 96 (2012) 657–667, https://doi.org/10.1016/j.saa.2012.07.037.

[57] S. Premkumar, A. Jawahar, T. Mathavan, M.K. Dhas, V.G. Sathe, A.M.F. Benial, DFT calculation and vibrational spectroscopic studies of 2-(tert-butoxycarbonyl (Boc)-amino)-5-bromopyridine, Spectrochim. Acta Mol. Biomol. Spectrosc. 129 (2014) 74–83, https://doi.org/10.1016/j.saa.2014.02.147.

[58] P. Divya, V.S. Jeba Reeda, S. Selvaraj, Bena Jothy, Theoretical spectroscopic electronic elucidation with polar and nonpolar solvents (IEFPCM model), molecular docking and molecular dynamic studies on bendiocarb-antiallergic drug agent, J. Mol. Liq. 404 (2024) 124895, https://doi.org/10.1016/j.molliq.2024.124895.

[59] R.V. Kabilan, C. Arunagiri, G.R. Ramkumaar, K. Sathyamoorthy, C. Karnan, Combined experimental and theoretical investigations on 9-[3, 4-dihydroxy-5-(hydroxymethyl) oxolan-2-yl]-1, 9-dihydro-6H-purin-6-one 4-nitrophenol (IPNP) molecule, J. Mol. Struct. 1263 (2022) 133020, https://doi.org/10.1016/j.molstruc.2022.133020.

[60] Y. Sert, M. Gumuş, H. Gokce, I. Kani, I. Koca, Molecular docking, Hirshfeld surface, structural, spectroscopic, electronic, NLO and thermodynamic analyses on novel hybrid compounds containing pyrazole and coumarin cores, J. Mol. Struct. 1171 (2018) 850–866, https://doi.org/10.1016/j.molstruc.2018.06.069.

[61] A. Ammasi, X.H. Ju, The influence of metal-free thiophene spacer chain on optoelectronic analysis by TD-DFT method for efficient dye-sensitized solar cells with enhanced non-linear optical activity, J. Phys. Chem. Solid. 193 (2024) 112155, https://doi.org/10.1016/j.jpcs.2024.112155.

[62] M. Djeribi, I. Nagazi, V. Cocetta, N. Dege, N. Issaoui, L. Zanetti, M. Carraro, B. Ayed, Synthesis of novel supramolecular selenomolybdate as anticancer agents: an experimental and DFT computational analysis, J. Mol. Struct. 1306 (2024) 137880, https://doi.org/10.1016/j.molstruc.2024.137880.

[63] A. Arunkumar, X.H. Ju, Computational method on highly efficient D-π-A-π-D-based different molecular acceptors for organic solar cells applications and non-linear optical behaviour, Spectrochim. Acta Mol. Biomol. Spectrosc. 317 (2024) 124391, https://doi.org/10.1016/j.saa.2024.124391.

[64] C.A. Lipinski, F. Lombardo, B.W. Dominy, P.J. Feeney, Experimental and computational approaches to estimate solubility and permeability in drug

discovery and development settings, Adv. Drug Deliv. Rev. 64 (2012) 4–17, https://doi.org/10.1016/j.addr.2012.09.019.

[65] E. Mohanapriya, S. Elangovan, N. Kanagathara, M.K. Marchewka, J. Janczak, P. Revathi, P, Density functional theory calculations, structural and spectroscopic characterization, and solvent-dependent HOMO-LUMO studies of 2-nitro-4-methylanilinium benzenesulfonate, J. Mol. Struct. 1317 (2024) 139147, https://doi.org/10.1016/j.molstruc.2024.139147.

[66] S. Akshay Kalyan, N. Kanagathara, M.K. Marchewka, Jan Janczak, K. Senthilkumar, Structure, Spectroscopy, and Theoretical insights on Co-crystals of 2, 4-Diamino-6-Methyl-1, 3, 5-Triazine Bis (4-Aminobenzoic acid) Monohydrate as a promising anti-cancer agent, Phys. B Condens. Matter 679 (2024) 415807, https://doi.org/10.1016/j.physb.2024.415807.